Motoneuron-driven computational muscle modelling with motor unit resolution and subject-specific musculoskeletal anatomy

Abbreviated title: Motoneuron-driven muscle modelling

Arnault H. Caillet[1,2], Andrew T.M. Phillips[1], Dario Farina[2,*], Luca Modenese[1,3*]

[1]Department of Civil and Environmental Engineering, Imperial College London, SW7 2AZ, UK
[2]Department of Bioengineering, Imperial College London, SW7 2AZ, UK
[3]Graduate School of Biomedical Engineering, University of New South Wales, Sydney 2052, Australia

Emails: arnault.caillet17@imperial.ac.uk; d.farina@imperial.ac.uk; l.modenese@unsw.edu.au

* These authors have equal contributions and share the senior authorship

CONFLICT OF INTEREST STATEMENT: The authors declare no competing financial interests.

Abstract

The computational simulation of human voluntary muscle contraction is possible with EMG-driven Hill-type models of whole muscles. Despite impactful applications in numerous fields, the neuromechanical information and the physiological accuracy such models provide remain limited because of multiscale simplifications that limit comprehensive description of muscle internal dynamics during contraction. We addressed this limitation by developing a novel motoneuron-driven neuromuscular model, that describes the force-generating dynamics of a population of individual motor units, each of which was described with a Hill-type actuator and controlled by a dedicated experimentally derived motoneuronal control. In forward simulation of human voluntary muscle contraction, the model transforms a vector of motoneuron spike trains decoded from high-density EMG signals into a vector of motor unit forces that sum into the predicted whole muscle force. The control of motoneurons provides comprehensive and separate descriptions of the dynamics of motor unit recruitment and discharge and decode the subject's intention. The neuromuscular model is subject-specific, muscle-specific, includes an advanced and physiological description of motor unit activation dynamics, and is validated against an experimental muscle force. Accurate force predictions were obtained when the vector of experimental neural controls was representative of the discharge activity of the complete motor unit pool. This was achieved with large and dense grids of EMG electrodes during medium-force contractions or with computational methods that physiologically estimate the discharge activity of the motor units that were not identified experimentally. This neuromuscular model advances the state-of-the-art of neuromuscular modelling, bringing together the fields of motor control and musculoskeletal modelling, and finding applications in neuromuscular control and human-machine interfacing research.

Author Summary

Neuromuscular computational simulations of human muscle contractions are typically obtained with a mathematical model that transforms an electromyographic signal recorded from the muscle into force. This single-input single-output approach, however, limits the comprehensive description of muscle internal dynamics during contraction because of necessary multiscale simplifications. Here, we advance the state-of-the-art in neuromuscular modelling by proposing a novel mathematical model that describes the force-generating dynamics of the individual motor units that constitute the muscle. For the first time, the control to the population of modelled motor units was inferred from decomposed high-density electromyographic signals. The model was experimentally validated, and the sensitivity of its predictions to different experimental neural controls was assessed. The neuromuscular model, coupled with an image-based musculoskeletal model, includes a novel and advanced neuromechanical model of the motor unit excitation-contraction properties, and is suited for subject-specific simulations of human voluntary contraction, with applications in neurorehabilitation and the control of neuroprosthetics.

Introduction

During voluntary skeletal muscle contractions, the pool of alpha-motoneurons (MNs) and the muscle fibres they innervate, constituting the muscle's population of motor units (MUs), transform in a series of chemical-mechanical events the neural message from the spinal cord into molecular forces (Huxley & Niedergerke, 1954). These forces sum across the multiscale architecture of the muscle to build the individual MU forces and the whole muscle force. Extensive experimental investigations in animals *in vivo* have advanced our understanding of the neuromechanical dynamics responsible for voluntary muscle contraction. For example, the force generated by skeletal muscles is modulated by the discharge frequencies of the innervating MNs (Heckman & Enoka, 2012), and by the number of discharging MUs, which are sequentially recruited in the increasing order of their size and the force they can generate (Henneman, 1981; Caillet et al., 2022b). Because invasive *in vivo* practices in humans are reduced to specific electrode insertions (Van Cutsem et al., 1997; Muceli et al., 2022) or challenging surgeries (Gollapudi & Lin, 2009; Ferguson & Shur, 2022; Binder-Markey et al., 2023), our understanding of human voluntary muscle contraction mainly relies on non-invasive *in vivo* techniques, such as bipolar (bEMG) and high-density (HDEMG) surface electromyography (De Luca, 1997; Del Vecchio et al., 2020; Waasdorp et al., 2021), imaging (Pincheira et al., 2022; Dick & Hug, 2023), and joint torque recordings. These non-invasive techniques are however challenging to apply during real-time contractions on multiple muscles, provide limited information that is usually not easily interpreted, or are commonly constrained to simple tasks like isometric contractions. When some neuromuscular properties and dynamics cannot be measured in humans, they are often extrapolated from animals, despite important limitations (Manuel et al., 2019; Highlander et al., 2020; Binder-Markey et al., 2023).

To support experimental investigations into understanding and simulating the interplay between human motor control and force generation, mathematical models of skeletal muscles were developed to mimic the dynamics of muscle contraction. Hill-type neuromuscular models are popular solutions which have been extensively reviewed recently (Caillet et al., 2022c). They rely on few parameters, are computationally cheap and conceptually simple, while complex enough to describe the chain of neuromechanical events responsible for muscle force generation, which makes them accurate, flexible and capable of refinement (Schmitt et al., 2019). Hill-type models have been used to explore voluntary neuromuscular control with EMG-driven forward simulations of muscle contraction (Hof & Van den Berg, 1981; Lloyd & Besier, 2003; Pizzolato et al., 2015; Sartori et al., 2017; Kapelner et al., 2020). With these methods, the recorded EMG signals are processed to provide a unique neural control to a single Hill-type actuator that phenomenologically describes whole muscle dynamics. This approach is well-established and implemented in automated tools (Pizzolato et al., 2015) and has had important

applications, for example in human-machine interfacing (Sartori et al., 2012; Ao et al., 2017; Caggiano et al., 2022; Cimolato et al., 2022).

However, and despite attempts to address this limitation (Hatze, 1977; Dorgan & O'Malley, 1997; Song et al., 2008; Dick, Taylor J. M. et al., 2017; Hussein et al., 2021), this single-input approach lumps the recruitment and discharge dynamics of the muscle's individual MUs into a unique phenomenological neural control for the whole MU population, the resulting force-generating events of which are hence lumped into single representative quantities for the whole MU pool. These representative quantities usually overlook the continuous distribution of the MUs' neuromechanical properties across the MU pool and are difficult to calibrate and interpret (Hussein et al., 2022). Consequently, this single-actuator macroscopic approach does not provide an adequate structure to physiologically describe the independent and inter-related (cail; Lubel et al., 2023; Hug et al., 2023) dynamics of a muscle's MU pool. These limitations hinder the investigation of human neuromuscular control with computational tools. In response to this limitation, other studies developed more physiological muscle models described as populations of Hill-type actuators, each of which simulated the dynamics of individual MUs (Hatze, 1980; Hamouda et al., 2016; Carriou et al., 2019). Yet, those models received synthetic motoneuronal signals and were not tested, and most of them not validated in conditions of voluntary neuromuscular control. Recent advances in the recording and decomposition of surface HDEMG signals (Negro et al., 2016; Caillet et al., 2023) allow the non-invasive identification of trains of action potentials for large samples of MUs discharging during human voluntary contraction. To date, those vectors of identified MU spike trains were systematically compiled into single neural controls to drive single Hill-type muscle actuators (Sartori et al., 2017; Kapelner et al., 2020). Consequently, the experimental spiking behaviour of the identified discharging MNs was never used to control Hill-type-like models of individual MUs in the simulation of human voluntary contraction.

To address this gap, in this study a novel MN-driven neuromuscular model was developed and validated. The model was described as a population of Hill-type actuators, each of which simulated the neuromechanical and force-generating dynamics of individual MUs. In forward simulations of human voluntary contraction, the MN-driven model transformed an experimental vector of MN spike trains decoded from HDEMG signals (Caillet et al., 2023), that comprehensively described the dynamics of MU recruitment and rate coding, into a vector of simulated MU forces that summed into the predicted whole muscle force. Sampling the muscle into individual MUs provided an adequate structure for proposing robust multiscale simplifications, advanced models of the MU activation dynamics, and physiological muscle-specific distributions of the MU's neuromechanical properties across the MU pool, that were scaled to subject-specific values derived from a subject-specific musculoskeletal (MSK) model. It was shown that accurate muscle force predictions were obtained when the experimental

motoneuronal controls accurately described the real discharge activity of the MU pool. This was obtained with experimental samples of MN spike trains derived from large and dense grids of EMG electrodes, and, to some extent, when the discharge activity of the complete MU pool was reconstructed from experimental data with computational methods (Caillet et al., 2022a). By proposing novel solutions for controlling and designing Hill-type-like neuromuscular models, this study advances the state-of-the-art of neuromuscular modelling, opens avenues for investigating the interplay between the CNS and the neuromuscular machinery during human voluntary contraction, reconciles the complementary fields of motor control and MSK modelling, and finds applications in neurorehabilitation and the design and control of neuroprosthetics (Farina et al., 2017; Farina et al., 2021).

Methods

1. Overview of MN-driven neuromuscular modelling

We developed an experimental and computational method (Figure 1) for simulating, with a MN-driven neuromuscular model, the neuromechanical dynamics of a subject-specific population of individual MUs during human voluntary isometric muscle contraction. From surface HDEMG signals recorded on the Tibialis Anterior (TA) muscle (Figure 1A, B), we decoded the experimental discharge activity of the population of identified MUs (Figure 1C), which was extended to the complete MU pool (Figure 1D) using an open-source computational method (Caillet et al., 2022a), available at https://github.com/ArnaultCAILLET/Caillet-et-al-2022-PLOS_Comput_Biol. The accuracy of both the experimental and reconstructed populations of spike trains $sp_i(t)$ in estimating the neural drive to muscle $\overline{D}(t)$ was validated (Figure 1E). We described the MN-driven neuromuscular model (Figure 1F) as a collection of in-parallel Hill-type Force Generators (FGs), each of which was controlled by a dedicated spike train $sp_i(t)$. Each FG described the neuromechanics of a MU and included a Neuromechanical Element (NE) and a Contractile Element (CE) to describe the excitation-contraction coupling properties (MU excitation and activation dynamics) and mechanical properties (MU contraction dynamics) of the MU, respectively (Caillet et al., 2022c). The FGs individually transformed the spike trains $sp_i(t)$ into the MU forces $f_i^{MU}(t)$ that collectively generated the whole muscle force $F^M(t)$ (Figure 1G). We further scaled the MN-driven neuromuscular model to be subject-specific with muscle-tendon properties derived from a subject-specific MSK model obtained from segmented magnetic resonance images (MRIs) (Figure 1H, I). We finally validated the predicted force $F^M(t)$ against a reference muscle force $F_{TA}(t)$ (Figure 1G), that was estimated (Figure 1J) from the recorded ankle torque $T(t)$ and the bipolar EMG (bEMG) activity of the TA's agonist and antagonist muscles crossing the ankle joint.

In the following, when subject-specific properties could not be measured *in vivo*, the coefficients of the mathematical equations describing the model were tuned with experimental data from the literature, considering in turn and decreasing order of preference experimental studies on individual human MUs or bundles of fibres, human fibres and sarcomeres, cat fibres, rodent fibres, rodent muscles, and amphibian fibres or muscles. Any experimental quantity measured at the sarcomere and/or fibre scales was directly assigned to the MU scale.

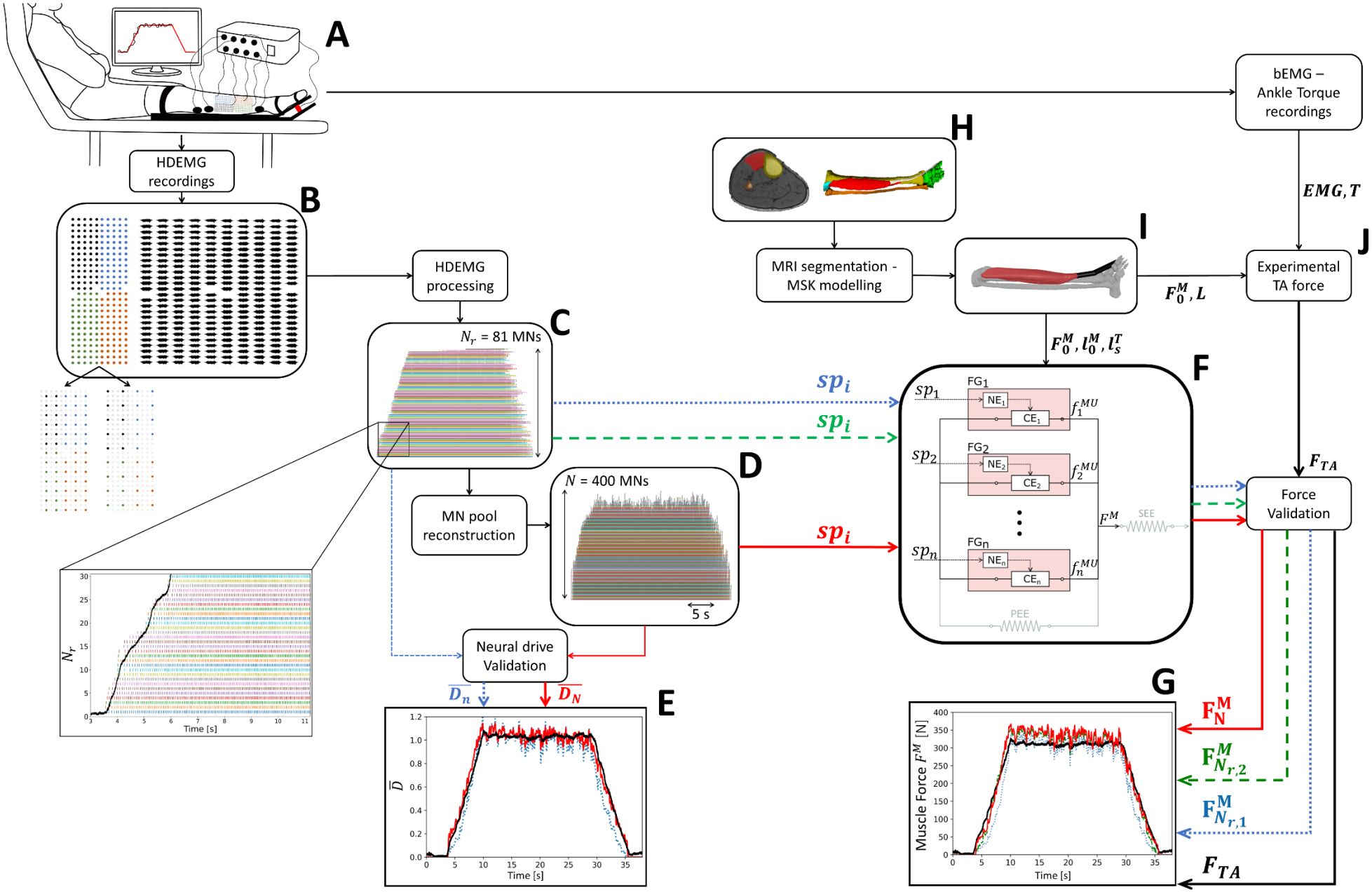
A
HDEMG recordings
B
HDEMG processing
C
N_r = 81 MNs
MN pool reconstruction
D
N = 400 MNs
5 s
Neural drive Validation
$\overline{D_n}$
$\overline{D_N}$
E
$\overline{D}$
Time [s]
N_r
Time [s]
bEMG – Ankle Torque recordings
EMG, T
H
MRI segmentation - MSK modelling
I
F_0^M, L
J
Experimental TA force
F_0^M, l_0^M, l_s^T
F
sp_i
sp_1
sp_2
sp_n
FG1
FG2
FGn
NE1
NE2
NEn
CE1
CE2
CEn
f_1^{MU}
f_2^{MU}
f_n^{MU}
F^M
SEE
PEE
F_{TA}
Force Validation
G
Muscle Force F^M [N]
Time [s]
F_N^M
$F_{N_{r,2}}^M$
$F_{N_{r,1}}^M$
F_{TA}

147

Figure 1: Description of the steps involved in the forward prediction and validation of the TA muscle force during isometric contractions using the developed subject-specific MN-driven neuromuscular model. During trapezoidal isometric ankle dorsiflexions (A), HDEMG signals were recorded from the TA muscle with a grid of 256 EMG electrodes, built with four grids of 64 electrodes (B), which was artificially downsampled into two grids of lower electrode density. Using convolutive blind-source separation, the HDEMG signals were decomposed into N_r identified motor unit spike trains (C), from which the discharge activity of the complete MU pool was inferred and reconstructed (D) (Caillet et al., 2022a). The experimental and reconstructed populations of spike trains $sp_i(t)$ were validated for their accuracy in estimating the normalized effective neural drive $\overline{D}(t)$ to muscle (E). The MN-driven neuromuscular model developed in this study (F), consists of a collection of in-parallel Hill-type MU Force Generators (FGs), each including a Neuromechanical Element (NE) and a Contractile Element (CE), that collectively generate the whole TA muscle force F^M. F^M was predicted (G) from the experimental sp_i(t) trains in a blind approach (blue dotted lines), after location of the identified MUs into the MU pool (green dashed lines), and from the completely reconstructed population of spike trains (solid red lines). The neuromuscular model was scaled with subject-specific muscle-tendon properties derived from a subject-specific MSK model (I), obtained from segmented MRI scans (H). The predicted TA force $F^M_{N_{r,1}}$, $F^M_{N_{r,2}}$, or F^M_N, depending on the type of neural control, was finally validated (G) against the experimental TA force F_{TA} (J). F_{TA} was estimated from the recorded ankle torque T and the estimated co-activity of the TA's agonist and antagonist muscles crossing the ankle joint.

2. Experimental data and subject-specific neuromusculoskeletal quantities

2.1. Contraction tasks, force and EMG recordings, and subject-specific spiking activity

The experimental approach represented in Figure 1A was described elsewhere (Caillet et al., 2023) and is briefly summarized here. One healthy male participant (age: 26 yr; height: 168 cm; body weight: 52 kg) volunteered to participate in the experimental session of the study. The participant sat on a massage table with the hips flexed at 30°, 0° being the hip neutral position, and his knees fully extended and strapped to the massage table to avoid any knee and hip motion and co-contraction of the thigh muscles during the ankle dorsiflexion. The ankle torque signals $T(t)$ were recorded with a load cell (CCT Transducer s.a.s, Turin, Italy) connected in-series to the pedal of a commercial dynamometer (OT Bioelettronica, Turin, Italy), to which the participant's foot was fixed at 30° in the plantarflexion direction, 0° being the foot perpendicular to the shank. The effects of gravity, including the rig weight, were cancelled by removing the initial measured offset during the experiments. After registering the participant's maximum voluntary contraction (MVC) in dorsiflexion, the participant performed two trapezoidal isometric contractions at 30% and 50% MVC with 120 s of rest in between, consisting of linear ramps up and down performed at 5%/s and a plateau maintained for 20 s and 15 s at 30% and 50% MVC, respectively.

To derive subject-specific motoneuronal controls to the neuromuscular model, HDEMG signals were recorded over the TA muscle during a first experimental session with a total of 256 EMG electrodes (Figure 1B), distributed between four rectangular grids of 64 electrodes, with 4 mm interelectrode distance covering 36 cm^2 of the muscle surface (10 cm x 3.6 cm; OT Bioelettronica). HDEMG and force signals were recorded using the same acquisition system (EMG-Quattrocento; OT Bioelettronica) with a sampling frequency of 2,048 Hz. As previously described (Caillet et al., 2023), the 256-electrode grid was downsampled by successively discarding rows and columns of electrodes and artificially generating two new grids of lower electrode density (Figure 1B). The two grids covered the same muscle area with interelectrode distance of 8 mm and 12 mm, involving 64 and 36 electrodes, respectively. After visual inspection and band-pass filtering, the HDEMG signals recorded with the three grids were decomposed into motor unit spike trains using convolutive blind-source separation, as previously described (Negro et al., 2016). After the automatic identification of the motor units, duplicates were removed, and all the motor unit spike trains were visually checked for false positives and false negatives (Del Vecchio et al., 2020). Only the motor units which exhibited a pulse-to-noise ratio > 28 dB were retained for further analysis. The final N_r spike trains $sp_i(t)$ identified experimentally (Figure 1C) were stored as binary vectors of zeros and ones identifying the sample times when a discharge occurred. The ankle torques T^{th} at which the N_r MUs were recruited, also called *torque recruitment thresholds* in the following, were calculated as the average of the recorded T values

192 over a 10 ms range centred around the MUs' first identified discharge time. In the following, the N_r
193 MUs identified experimentally were ranked in the ascending order of measured recruitment torques
194 T_i^{th} with the index $i \in [\![1; N_r]\!]$. According to the Henneman's size principle (Henneman, 1981; Caillet
195 et al., 2022b), these MUs were therefore also ranked in the same order of current recruitment
196 threshold I_{th}, maximum isometric forces f_0^{MU}, and innervation ratios IR according to EQ. 1.

$$\forall j, k \in [\![1; N_r]\!], j < k \Leftrightarrow I_{th}(j) < I_{th}(k) \Leftrightarrow T^{th}(j) < T^{th}(k) \Leftrightarrow f_0^{MU}(j) < f_0^{MU}(k) \Leftrightarrow IR(j) < IR(k) \quad \text{EQ. 1}$$

197

198 In a second session where the isometric contractions were repeated following the same protocol,
199 bEMG signals were recorded from the pair of agonist extensor digitorum longus (EDL) and extensor
200 hallucis longus (EHL) muscles, and from the antagonist Gastrocnemius Medialis (GM) and Lateralis (GL),
201 and Soleus (SOL) muscles with adhesive bipolar electrodes (OT Bioelettronica). During this second
202 session, the participant additionally produced two MVCs in plantarflexion. The bEMG signals were
203 band-pass filtered (10-450 Hz), full-wave rectified, and then low-pass filtered (2 Hz) (Sartori et al.,
204 2017), before the resulting envelopes were normalized with respect to the peak processed EMG values
205 obtained in the MVC trials.

206

207 ### 2.2. MRI scans, subject-specific MSK quantities, and experimental force estimation

208 To scale the neuromuscular model to subject-specific MSK quantities, a 3D T1-weighted VIBE
209 (volumetric interpolated breath-hold examination) sequence was used to acquire high resolution
210 images (0.45 x 0.45 mm pixel size, 1 mm slice thickness and increment) from the knee joint to mid-foot
211 of the participant's dominant leg. The sequence consisted in three blocks with 50 mm overlap, during
212 which the participant was asked not to move to facilitate a successful merging of the adjacent blocks.

213 The volumetric shapes of the tibia, fibula, and foot bones, and of the TA muscle belly and tendon were
214 carefully identified by manual segmentation (Figure 1H) using ITK-SNAP (Yushkevich et al., 2006) and
215 an anatomical atlas as support (Möller & Reif, 2007). Slices of the agonist EDL and EHL and antagonist
216 SOL, GM, and GL muscle bellies were segmented at regular intervals along the tibial length so that their
217 centroidal lines of action could be outlined. All the main tendons crossing the ankle joint could be
218 clearly identified and were fully segmented. An expert radiologist confirmed the accuracy of the
219 segmentation. The segmented shapes were manually adjusted on the transversal plane to avoid
220 inconsistency of the muscle geometry in correspondence of the MRI sequence blocks using Netfabb
221 (https://www.autodesk.com/products/netfabb/) and Meshlab (Cignoni et al., 2008). The TA muscle

volume V^M computed from the segmentation was found consistent with the relationships between anthropometry and muscle volumes proposed by Handsfield et al. (2014) from a cohort of segmented MRI scans. Therefore, the volume V^M of the EDL, EHL, SOL, GM, GL muscle bellies was estimated with the volume-height-mass relationship provided in the supplementary material of Handsfield et al. (2014).

A subject-specific skeletal model of the ankle joint compatible with OpenSim (version 4.4) (Delp et al., 2007; Seth et al., 2018) was automatically generated from the segmented bone volumes (Figure 1I) using the open-source automated toolbox STAPLE (Modenese & Renault, 2021). With this approach, the ankle joint was modelled as a hinge joint, the axis of rotation of which was personalised based on the shape of the articular surfaces of the segmented talus bone. Using another automated approach (Modenese & Kohout, 2020), the centroidal line of action of TA was automatically computed from the segmented muscle geometry. Similarly, the centroidal lines of action for EDL, EHL, SOL, GM, and GL were manually outlined from the segmented muscle slices. The muscle tendons paths were manually defined in NMSBuilder (Valente et al., 2017) using the segmented tendons as reference.

To reproduce the experimental conditions, the plantarflexion angle of the final subject-specific MSK model was set to 30°. At this angle, the subject-specific muscle-tendon length l^{MT} of the six muscles and their moment arm L with respect to the ankle joint were computed using OpenSim. The subject-muscle-specific optimal length l_0^M and the tendon slack length l_s^T of the six muscles were estimated from the muscle-specific values $l_{0,Raj}^M$ and $l_{s,Raj}^T$ proposed in a generic published model (Rajagopal et al., 2016), which were scaled with EQ. 2 by maintaining their ratio with respect to the entire musculotendon lengths l_{Raj}^{MT} and l^{MT} in the neutral ankle position.

$$\begin{cases} l_0^M = \dfrac{l^{MT}}{l_{Raj}^{MT}} \cdot l_{0,Raj}^M \\ l_s^T = \dfrac{l^{MT}}{l_{Raj}^{MT}} \cdot l_{s,Raj}^T \end{cases} \qquad \text{EQ. 2}$$

Considering a specific tetanic tension of $\sigma = 60\ N/cm^2$ (Rajagopal et al., 2016), the subject-specific maximum isometric force F_0^M of the six muscles was obtained from the known muscle volumes V^M with EQ. 3.

$$F_0^M = \frac{V^M}{l_0^M} \cdot \sigma \qquad \text{EQ. 3}$$

Combining these subject-muscle-specific properties with the bEMG signals recorded from the co-contracting flexor muscles during the second experimental session (Figure 1A), the experimental force $F_{TA}(t)$ developed by the TA during the first experimental session was inferred (Figure 1J) from the

measured experimental ankle torque $T(t)$ with EQ. 4. In EQ. 4, L_{TA} is the moment arm the TA tendon makes with the ankle joint, and $\Delta T(T)$ relates the level of measured ankle torque $T(t)$ to the algebraic amount of ankle torque ΔT taken by the group of agonist EHL and EDL and antagonist SOL, GM, and GL muscles. The continuous $\Delta T(T)$ relationship was obtained by trendline fitting the $(T; \Delta T)$ cloud of points measured during the second experimental session. Details on ttohe calculation of $\Delta T(T)$ are provided in Appendix A.1.

$$F_{TA}(t)[N] = \frac{T(t) - \Delta T\big(T(t)\big)}{L_{TA}} \qquad \text{EQ. 4}$$

3. Generic properties of the MU pool in the human TA muscle

From an extensive review of the experimental human TA literature performed elsewhere (Caillet et al., 2022a), it was assumed that a typical adult TA muscle included N_f^{tot} =200,000 muscle fibres gathered into $N = 400$ Mus. This review also returned that the TA MU torque recruitment thresholds T^{th}, expressed in percentage of the maximum recorded torque (% MVC), followed the generic linear-exponential continuous distribution in EQ. 5 and displayed in Figure 2A. In EQ. 5, j is an integer identifying the jth MU in the entire pool ranked in the ascending order of MU torque recruitment thresholds.

$$T^{th}(j) = 0.50 \cdot \left(58.12 \cdot \frac{j}{N} + 120^{\left(\frac{j}{N}\right)^{1.83}}\right), j \in [\![1; N]\!] \qquad \text{EQ. 5}$$

The N_r MUs identified in the experimental trials were ranked with the index i ($i \in [\![1; N_r]\!]$, with $N_r < N$) in the ascending order of measured T_i^{th}. Using the $T^{th}(j)$ distribution in EQ. 5, these experimental MUs were mapped into the complete T^{th}-ranked pool of 400 MUs, where they were assigned a new index N_i ($N_i \in [\![1; N]\!]$), as shown in EQ. 6. To do so, the equation $T_i^{th} = T^{th}(N_i)$ was solved for the unknown N_i for the N_r experimental MUs.

$$i \in [\![1; N_r]\!] \rightarrow N_i \in [\![1; N]\!] \qquad \text{EQ. 6}$$

Never measured in human muscles *in vivo*, the continuous distribution of the normalized MU maximum isometric forces $\overline{f_0^{MU}}(j)$ in the TA was here approximated from a continuous distribution $\overline{f^{tw}}(j)$ of MU twitch force normalized to the muscle maximum isometric force F_0^M. Processing published experimental TA data (Andreassen & Arendt-Nielsen, 1987; Van Cutsem et al., 1997; Van Cutsem et al., 1998) with the same method as used for EQ. 5, EQ. 7 was obtained. In EQ. 7, a 16.3-fold range was taken for the f^{tw} values, consistently with Figure 3a in Van Cutsem et al. (1997) for a single

subject, as opposed to a 250-fold range proposed in a recent review (Duchateau & Enoka, 2022) that relied on the same figure, but considering unnormalized merged data from ten subjects.

$$\overline{f^{tw}}(j) = 6.07 \cdot \left(4.52 \cdot \frac{j}{N} + 11.96^{\left(\frac{j}{N}\right)^{4.66}}\right), \ \mathrm{j} \in [\![1; N]\!] \qquad \text{EQ. 7}$$

The normalized $\overline{f_0^{MU}}(j)$ distribution in EQ. 8 was then estimated by scaling the coefficients in EQ. 7 to obtain a 11-fold range for the $\overline{f_0^{MU}}$ values in the TA MU pool, to account for the different twitch-tetanus ratios obtained between slow and fast fibres in the rodent literature (Celichowski & Grottel, 1993). In EQ. 8, $\sum_{j=1}^{N} \overline{f_0^{MU}}(j) = 1$. The $f_0^{MU}(j)$ distribution in Newtons, displayed in Figure 2B, is finally obtained by multiplying EQ. 8 by the F_0^M value obtained with EQ. 3.

$$\overline{f_0^{MU}}(j) = 7.86 \cdot 10^{-4} \cdot \left(3.00 \cdot \frac{j}{N} + 8.20^{\left(\frac{j}{N}\right)^{5.29}}\right), \ i \in [\![\mathrm{j}; N]\!] \qquad \text{EQ. 8}$$

Human muscles also display a continuous distribution of slow-to-fast MU types in the MU pool. It is known that, in a human TA of $N = 400$ MUs, 72% of the N_f^{tot} =200,000 TA fibres are Type 1 'slow' fibres (Henriksson-Larsén et al., 1983). Considering that the innervation ratio IR of a MU is roughly proportional to the amplitude of the MU force twitch f^{tw} (Caillet et al., 2022b), EQ. 9 gives the continuous distribution of IR, displayed in Figure 2D.

$$IR(j) = \frac{\overline{f^{tw}}(j)}{\sum_{k=1}^{400} \overline{f^{tw}}(k)} \cdot N_f^{tot}, \ j \in [\![1; N]\!] \qquad \text{EQ. 9}$$

Although it is debated (Caillet et al., 2022b) whether the MU type, currently determined by the MU twitch force f^{tw}, is also correlated or not to the MU size, i.e., to the MU Force recruitment threshold in humans, it was here assumed that the small low-threshold MUs were of the 'slow' type, and the large high-threshold MUs of the 'fast' type. Therefore, from the cumulative summation of the MU IRs, the 359 lowest-threshold MUs that have the lowest innervation ratios were considered to account for 72% of $N_f^{tot}$and to be of the 'slow' type in the following.

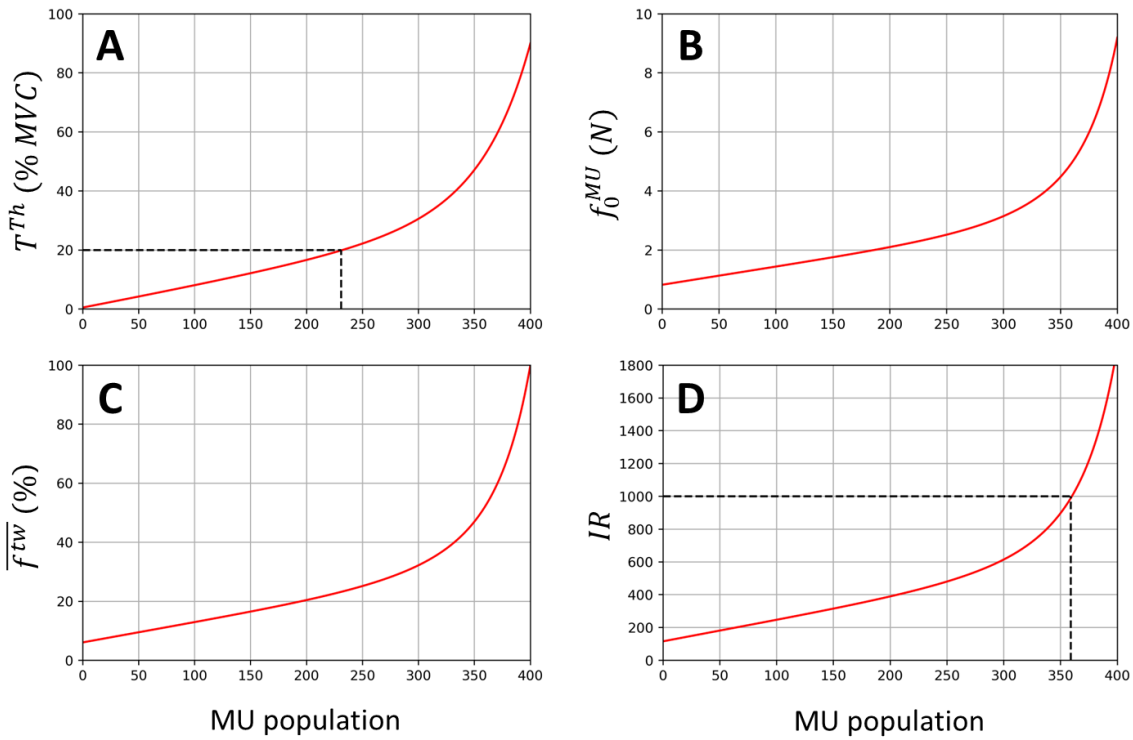

Figure 2: In a generic human TA muscle, distributions in the pool of $N = 400$ MUs of the MU torque recruitment thresholds T^{th} (A), MU maximum isometric forces f_0^{MU} (B), MU twitch forces $\overline{f^{tw}}$ normalized to the muscle maximum isometric force F_0^M and expressed in percentage (C), and MU innervation ratios IR (D), calculated with EQ. 5 to EQ. 9. (A) As identified by the dashed line, 231 TA MUs, i.e., 58% of the MU pool is recruited below 20% MVC, which is consistent with previous conclusions (Heckman & Enoka, 2012). (B) The normalized distribution in EQ. 8 was scaled to Newtons with the subject-specific maximum isometric force of the TA F_0^M derived previously. From the subject-specific moment arm of the TA derived previously, TA MUs are expected to produce 20 to $230 \cdot 10^{-3}$ Nm twitch torques with this distribution, which is consistent with the measurements reported in Van Cutsem et al. (1997). (D) As identified by the dashed line, the 359 smallest TA MUs gather 72% of the fibre constituting the muscle and are assumed slow-type MUs. According to EQ. 1, the MUs are ranked in the same ascending order of Fth, f_0^{MU}, $\overline{f^{tw}}$, and IR.

4. Development of a MN-driven neuromuscular model described as a population of Hill-type MU actuators

4.1. Rheological description and preliminary simplifications

The MN-driven neuromuscular model developed in this study (Figure 1F) consists of a population of n in-parallel FGs, that describe the force-generating activity of the MU pool with mathematical models of the individual MU's force-generating dynamics (Figure 3). n is the length of the vector of available input spike trains controlling the model and takes the values N_r or N in this study. Using step-by-step simplifications justified in detail in Appendix A.2, {1} the TA tendon was assumed rigid (tendon length set to the tendon slack length l_S^T (Millard et al., 2013)) and the in-series elastic element (SEE, in grey in

Figure 1F) and its passive force dynamics were neglected, {2} all the MU actuators were assigned the same optimal length, set as the muscle's l_0^M, and the same normalized constant length, set as $\bar{l} = 1.16$ according the subject-specific MSK measurements, {3} the Force-Velocity properties of the MUs were therefore neglected, and {4} the passive force of the CE was found negligible, so that the passive elastic element (PEE, in grey in Figure 1F) was neglected. With these assumptions, and after normalizing the state variables to the F_0^M and l_0^M parameters and reporting them with a bar, as described in Appendix A.2, the whole muscle dynamics in isometric contractions were described with EQ. 10. In EQ. 10, at time t and for a population of n modelled MUs, F^M is the whole muscle force in Newtons, $\overline{f_k^{MU}}$ is the normalized force developed by the kth MU ($k \in [\![1; n]\!]$), and $\overline{f_{k,0}^{MU}}$ is the MU-specific normalized maximum isometric force that the kth MU can develop. In EQ. 10, the MU active states $a_k(\bar{l})$ and Force-Length (FL) scaling factors $f_{FL}(a_k, \bar{l})$ were derived from the input spike trains $sp_k(t)$ and the common MU length $\bar{l}$ with six cascading mathematical models of the MU's excitation, activation, and contraction dynamics summarized in Figure 3. Finally, because the MUs build force upon the discrete activity of their $IR_k = N_f^{tot} \cdot \overline{f_{k,0}^{MU}}$ fibres that receive the same MN action potential with a random time delay α_c, the calculation of the normalized MU forces $\overline{f_k^{MU}}$ in EQ. 10 was updated to $\overline{F_k^{MU}}$ to account for this non-simultaneous twitch activity, which acts as a low-pass filter.

$$F^M(t) = F_0^M \cdot \overline{F^M}(t)$$

$$\overline{F^M}(t) = \sum_{k=1}^{n} \overline{F_k^{MU}}(t)$$

$$\overline{F_k^{MU}}(t) = \frac{1}{IR_k} \cdot \sum_{c=0}^{IR_k} \overline{f_k^{MU}}(t + \alpha_c), \qquad \alpha_c \in \left[-\frac{\Delta t}{2}; \frac{\Delta t}{2}\right] \qquad \text{EQ. 10}$$

$$\overline{f_k^{MU}}(t) = \overline{f_{k,0}^{MU}} \cdot \left(a_k(t, \bar{l}) \cdot f_{FL}(t, a_k, \bar{l})\right)$$

$$\bar{l} = 1.16$$

For improved readability, the subscript k was discarded in the following of the Methods section to refer to the dynamics of a representative MU of the pool.

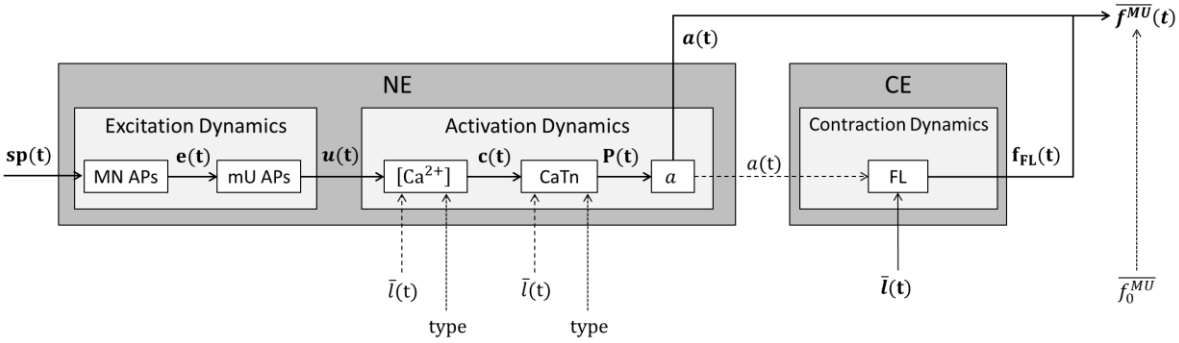

Figure 3: For a representative MU of the pool of Hill-type MUs in Figure 1F, description of the cascading dynamics that transform an input spike train $sp(t)$ into a normalized MU force $\overline{f^{MU}}(t)$. The time-history of $\overline{f^{MU}}(t)$ is obtained with EQ. 10 by product of the scaling factor $f_{FL}(t)$, the MU active state $a(t)$, and the MU normalized isometric force $\overline{f_0^{MU}}$. f_{FL} is obtained with a normalized FL relationship (Figure 4A) that entirely describes the Contraction Dynamics of the Contractile Element (CE) in isometric conditions. The Neuromechanical Element (NE) is controlled by the binary spike train $sp(t)$, which predicts during the MU's Excitation Dynamics the trains of motoneuron (MN) and muscle Unit (mU) Action Potentials (APs) in Volts (Figure 4B), identified with the $e(t)$ and $u(t)$ state variables, respectively. The discharge activity $u(t)$ triggers the MU's activation dynamics by successively controlling, with the $c(t), P(t)$ and $a(t)$ state variables, the concentration in Mols of free calcium ions ($[Ca^{2+}]$) in the sarcoplasm (Figure 4C-F), the concentration in Mols of the Calcium-Troponin complex (CaTn) in the sarcomeres, and the MU active state a. The interplay between the MU's NE and CE is modelled with a nonlinear dependency (dashed arrows) of the MU's Activation and Contraction Dynamics to the MU's length $\bar{l}(t)$ and activation $a(t)$, respectively. The MU's force-generating capacities also depend on some MU-specific properties (dotted lines), including its type (slow/fast) and its normalized isometric force $\overline{f_0^{MU}}$.

4.2. Contractile Element and Contraction Dynamics - MU Force-Length scaling factor f_{FL}

The MU f_{FL} scaling factor in EQ. 10 was defined with a normalized FL relationship and entirely describes the MU's contraction dynamics (Figure 3). To the authors' knowledge, no FL relationship was measured at the MU scale in humans. Despite limitations related to the multiscale approach (Caillet et al., 2022c), a human Force – Sarcomere Length relationship obtained from measurements in skinned human fibres (Gollapudi & Lin, 2009) was here considered the most suitable option. The sarcomere-to-MU multiscale assumption is here acceptable as muscles modelled as a scaled sarcomere for their normalized isometric FL properties can provide accurate Hill-type model predictions for mammalian whole muscles (Winters et al., 2011). Other available solutions were considered less appropriate, such as torque-length and torque-angle measurements in humans which are affected by muscle-tendon dynamics and muscle co-contraction, or FL measurements from fibre bundles in cat, rabbit and rat specimens, that have different optimal sarcomere lengths than humans (Burkholder & Lieber, 2001). Rather than a piecewise linear relationship consistent with the sliding filament theory at the sarcomere scale (Gordon et al., 1966), a gaussian mathematical description in EQ. 11 was fitted to the FL experimental data (red curve and black dots in Figure 4A) to account for the smoother relationship with larger plateau observed at larger scales (Hatze, 1980; Moo et al., 2020). For higher physiological credibility and improved prediction accuracy (Sun et al., 2018), the MU FL relationships were made

nonlinearly dependent to the MU activation states $a(t)$ (Lloyd & Besier, 2003) in EQ. 11 at submaximal contraction levels (dashed lines in Figure 4A).

$$f_{FL}(\bar{l}, a) = \exp\left(-\left(\frac{\bar{l} - \bar{l}_0(a)}{0.45}\right)^2\right) \qquad \text{EQ. 11}$$

$$\bar{l}_0(a) = 0.15(1 - a) + 1$$

4.3. MU Excitation Dynamics

Dynamics of MN AP elicitation

The time-history of the MU active state $a(t)$ in EQ. 10 was inferred by first transforming the input binary train of MN spikes $sp(t)$ into a train $e(t)$ of MN action potentials (APs) (Figure 3). The MN APs were phenomenologically modelled with EQ. 12 as analytical sine waves (Hatze, 1977) of half period $\frac{T}{2}$ and voltage amplitude V_e. The waves are triggered at the discharge times t_i when $sp(t = t_i) = 1$, while the MN membrane remains at equilibrium, i.e., $e(t) = 0$ for $t \notin \left[t_i; t_i + \frac{T}{2}\right]$. The individual AP shapes recorded in the literature of anesthetized and dissected cats previously reviewed (Caillet et al., 2022b) were fitted with EQ. 12, yielding $V_e = 90mV$ and $T = 1.4ms$ (Table 1). T is here shorter (Figure 4B) than the amphibian $T = 2ms$ (Ebashi & Endo, 1968) used in a previous neuromuscular model (Hatze, 1977).

$$\begin{cases} sp(t = t_i) = 1 \\ e(t) = \mathrm{V}_e \sin\left[\frac{2\pi}{T}(t - t_i)\right] & \text{for} \quad t_i \leq t \leq t_i + \frac{T}{2} \\ e(t) = 0 & \text{otherwise} \end{cases} \qquad \text{EQ. 12}$$

Dynamics of fibre AP elicitation

The train of the fibre APs ($u(t)$ in Figure 3) was modelled in EQ. 13 as the 2nd-order response (Hatze, 1977) to the train $e(t)$ of MN APs. In EQ. 13, when the fibre receives an isolated MN discharge, a_1 determines the peak-to-peak amplitude A_p of the fibre AP, while a_2 and a_3 respectively determine its time-to-peak duration t_{tp} and exponential decay time constant τ_d. The fibre APs simulated with the tuned a_i coefficients in Table 1 matched typical experimental cat values for A_p (77 mV), t_{tp} (0.6 ms) and τ_d (0.6 ms) (Farmer et al., 1960; Brooks & Hongdalarom, 1968; Ludin, 1969; Kopec et al., 1978; Wallinga-De Jonge et al., 1985; Wolters et al., 1994; Balog et al., 1994; Dillmann et al., 1996; Dumitru & King, 1999; Arabadzhiev et al., 2005; Kim et al., 2013), and were five times shorter (Figure 4B) than previously proposed for amphibians at low temperature (Hatze, 1977).

$$\frac{d^2u}{dt^2} = a_1 e(t) - \left(a_2 u + a_3 \frac{du}{dt}\right) \quad \text{EQ. 13}$$

4.4. MU Activation Dynamics

Dynamics of free calcium concentration

The MU excitation state $u(t)$ was modelled to control the level $c(t)$ of calcium concentration $[Ca^{2+}]$ in the MU sarcoplasm (Figure 3) with the 2nd-order ODE in EQ. 14, although alternative reviewed approaches were previously proposed (Caillet et al., 2022c). In EQ. 14, when the fibre receives an isolated fibre AP, b_1 determines the peak-to-peak amplitude A_c of the $[Ca^{2+}]$ twitch, and b_2 and b_3 its time-to-peak duration t_{tp} and decay time constant τ_d. The equation proposed in Hatze (1977) was modified to introduce the length-dependent scaling factors $f_1(\bar{l})$ and $f_2(\bar{l})$, defined in EQ. 15 and EQ. 16, that respectively make A_c and τ_d nonlinearly dependent to the normalized MU length $\bar{l}$. The procedure taken to tune the c_i coefficients and derive the $f_i(\bar{l})$ scaling factors to match available experimental data for amphibian and mammal slow and fast fibres *in vitro* is reported in Appendix A.3.

$$\frac{d^2c}{dt^2} = b_1 \cdot u(t) - \frac{1}{f_1(\bar{l})}\left(b_2 \cdot f_2(\bar{l}) \cdot c + b_3 \cdot \frac{dc}{dt}\right) \quad \text{EQ. 14}$$

$$\begin{cases} f_1(\bar{l}) = 0.8 & if\ \bar{l} \leq 1.0 \\ f_1(\bar{l}) = 0.8 + 1.33(\bar{l} - 1.0) & if\ \bar{l} \leq 1.15 \\ f_1(\bar{l}) = 1.0 & if\ \bar{l} \leq 1.30 \\ f_1(\bar{l}) = 1.0 - 0.6(\bar{l} - 1.3) & if\ \bar{l} > 1.30 \end{cases} \quad \text{EQ. 15}$$

$$\begin{cases} f_2(\bar{l}) = 1.0 & if\ \bar{l} \leq 1.15 \\ f_2(\bar{l}) = 1.0 - 0.4 \cdot (\bar{l} - 1.15) & if\ \bar{l} > 1.15 \end{cases} \quad \text{EQ. 16}$$

As reported in Figure 4D for fast fibres, the calcium transients simulated with the tuned b_i coefficients (Table 1) compared well with the experimental trace at 125 Hz stimulation from Hollingworth et al. (1996) once steady-state was reached. The calcium twitches at steady-state returned the expected $t_{tp} = 2.0ms$, $\tau_d = 6.6ms$, and $A_c = 20\mu M$ with less than 5% difference. As EQ. 14 does not account for some physiological mechanisms, such as receptor saturation and the CASQ-Traidin-RYR1 action, the typically larger A_c and τ_d of the first experimental $[Ca^{2+}]$ twitch (Baylor, S. M. & Hollingworth, 2003) were underestimated. Experimental data for slow type rodent fibres were available in Baylor & Hollingworth (2003) at 16°C, but not at 35°C body temperature. In Hollingworth et al. (1996), A_c, t_{tp} and τ_d respectively increased by 26%, remained constant, and decreased by 56% when increasing the temperature from 16°C to 35°C for fast-type fibres. The A_c, t_{tp} and τ_d coefficients reported at 16°C (Baylor, S. M. & Hollingworth, 2003) were scaled to 35°C using the same scaling factors. As shown in

Figure 4C, the simulated calcium transients at 35°C for slow fibres under 67Hz stimulation compared well with the scaled experimental data with similar t_{tp}, and τ_d of 19 and 44ms and an average underestimation of A_c of 20%. The calcium twitches simulated at optimal fibre length with EQ. 14 and the parameter values in Table 1 have ten times shorter half-widths and 2.3 times lower amplitudes (Figure 4E, F) than the twitches obtained with Hatze's model (Hatze, 1977), which was calibrated on frog data at 9°C.

Dynamics of Calcium-Troponin concentration

The sarcomeric calcium-troponin (CaTn) binding-unbinding process was described with EQ. 17 to predict from the free calcium concentration c the time-course of the concentration P of the Ca-Tn structures in the sarcomeres (Figure 3). The initial description (Wexler et al., 1997) was extended to account for the nonlinear length-dependency of the CaTn transients with the $f_{3,4,5}(\bar{l})$ scaling factors. In EQ. 17, P_0 is the total troponin concentration in the myoplasm, and c_1, c_2 are respectively the forward and backward reaction rates of the Ca-Tn binding-unbinding process. When triggered by a unique calcium twitch, $\frac{P_0}{f_4(\bar{l})}$ scales the peak-to-peak amplitude A_t of the CaTn twitch, and $\frac{c_1}{f_3(\bar{l})}$ and $\frac{c_2}{f_5(\bar{l})}$ determine its time-to-peak t_{tp} and decay constant τ_d. The P_0, c_1, c_2 coefficients, originally calibrated to match experimental force data with a neuromuscular model (Wexler et al., 1997), were here tuned to match contemporary experimental data (Baylor, S. M. & Hollingworth, 2003; Hollingworth, Stephen et al., 2008) following a method described in Appendix A.4.

$$\frac{dP}{dt} = \frac{c_1}{f_3(\bar{l})} \cdot \left(\frac{P_0}{f_4(\bar{l})} - P \right) \cdot c^2 - \frac{c_2}{f_5(\bar{l})} \cdot P \qquad \text{EQ. 17}$$

The tuned P_0, c_1, c_2 coefficients reported in Table 1, with which the experimental A_t, t_{tp}, and τ_d quantities could be reproduced with EQ. 17 with less than 5% error at all experimentally measured lengths and for both fibre types, are strongly consistent with the typical coefficient values reported in the cited literature $c_1 = 3.6 \cdot 10^{12}\ M^{-2} \cdot s^{-1}$, $c_2 = 100\ s^{-1}$, and $P_0 = 2.2 \cdot 10^{-4}\ M$.

Dynamics of MU activation

The MU active state can be defined as the normalized instantaneous ratio of formed cross-bridges in the force-generating state in a population of myosin heads from a representative sarcomere (Caillet et al., 2022c). Although semi-phenomenological models of multi-state cross-bridge attachments (Zot & Hasbun, 2016) are available, a phenomenological model (Ding et al., 2000) was used to infer the MU active state a from the CaTn concentration P (Figure 3) to reduce the computational cost, the number

of parameters to tune, and the overall model complexity. In EQ. 18, d_1, d_2 and d_3 respectively control the amplitude A_a of the activation twitch, its time-to-peak t_{tp} and its time of half-relaxation $t_{0.5}$, and were tuned to match, lacking more suitable experimental measurements in the literature, the normalized experimental twitch torque or force recorded in individual human MUs in the TA muscle (Andreassen & Arendt-Nielsen, 1987; Van Cutsem et al., 1997; Van Cutsem et al., 1998) following a method described in Appendix A.5.

$$\frac{da}{dt} = d_1 \cdot P - \frac{a}{d_2 + d_3 \cdot P} \qquad \text{EQ. 18}$$

Because of the MU type-specificity of the $[Ca^{2+}]$ and CaTn dynamics modelled previously, a unique set of values was obtained for the tuned d_1, d_2 and d_3 coefficients (Table 1) for both slow and fast MUs, with less than 7% error in reproducing the experimental A_t, t_{tp} and $t_{0.5}$ quantities when simulating single activation twitches for both slow and fast MUs.

When receiving artificial excitatory spike trains at 2, 10, 15, 20, 25, 30, and 50 Hz, the NE of a slow-type MU at optimal length $\bar{l} = 1$ produced the activation traces in Figure 4G. As supported by previous findings in mammals (Heckman & Enoka, 2012), the simulated activation twitches fused for MN firing frequencies above 2Hz and the initial rate of increase of the MU active state was independent from discharge frequency, while the 0-to-0.8 rate of increase increased with higher firing frequencies from 3.5/s at 15Hz and 5.8/s at 50Hz. Consistent with previous findings (Milner-Brown et al., 1973), every new elicited activation twitch increased the MU activation level at steady-state by 100% at 5Hz, and only by 1% at 50Hz, following a negative exponential tendency with increasing MN discharge frequency.

Figure 4H displays the simulated steady-state activation-frequency relationship for both slow-type MUs (blue triangles) and fast-type MUs (red symbols). Despite obvious limitations but lacking experimental measurements of human activation states in the literature, those results were compared to the literature of experimental human muscle force and torque twitches. In Figure 4H, simulated twitch-tetanus ratios of 0.30 and 0.19 were obtained at steady-state for the simulated slow and fast-type MU active states, respectively. These ratios are of the same order of magnitude as those experimentally obtained for human hand muscles (range 0.1-0.3, (Thomas, C. K. et al., 1991; Macefield et al., 1996; Fuglevand et al., 1999)). The activation-frequency results for the simulated slow-type MUs compared relatively well with the findings from these experimental studies with a maximum difference of 30% at 15Hz with the extensor digitorum brevis (EDB) muscle data (Macefield et al., 1996) and less than 10% at all physiological frequencies above 5Hz with the data obtained from thenar muscles (Thomas, C. K. et al., 1991). Yet, the simulated rate of increase in a with firing frequency largely

underestimated the available experimental data for the fast-type MUs with up to 200% difference. The lack of available experimental human data of fast MU twitches prevents for now from deriving more advanced conclusions on the accuracy of the simulated MU active states.

4.5. Solving the dynamics of the MU pool

Working at fixed MU length $\bar{l} = 1.16$ for each of the n modelled MUs, the cascading ODEs in EQ. 12 to EQ. 18, that describe the MU-specific excitation and activation dynamics, were first numerically solved at each time step, yielding a vector of MU active state time-histories $a_i(t)$. Figure 4I, J displays the time-histories of the five state variables that describe the NE's activity at 1 and 30 Hz, respectively. An estimation of the MU normalized forces and of the whole muscle force was then obtained with EQ. 10.

Table 1: Coefficients scaling EQ. 12 to EQ. 18 that describe the MUs' Excitation and Activation dynamics for both slow-type and fast-type MUs. Those coefficients were tuned to match contemporary experimental data on mammals at body temperature.

		slow	fast	Unit
EQ. 12	T	1.4		s
	V_e	90		V
EQ. 13	a_1	$9 \cdot 10^7$		s^{-2}
	a_2	$5 \cdot 10^7$		s^{-2}
	a_3	$2 \cdot 10^4$		s^{-1}
EQ. 14	b_1	0.4	0.9	$M \cdot V^{-1} \cdot s^{-2}$
	b_2	$1.5 \cdot 10^5$	$4.3 \cdot 10^5$	s^{-2}
	b_3	$2.5 \cdot 10^3$	$2.4 \cdot 10^3$	s^{-1}

		slow	fast	Unit
EQ. 17	c_1	$6 \cdot 10^{12}$	$1 \cdot 10^{12}$	$M^{-2} \cdot s^{-1}$
	c_2	21	41	s^{-1}
	P_0	$1.7 \cdot 10^{-4}$	$3.8 \cdot 10^{-4}$	M
EQ. 18	d_1	$1.00 \cdot 10^5$		$M^{-1} \cdot s^{-1}$
	d_2	0.024		s^{-1}
	d_3	270		$M^{-1} \cdot s^{-1}$

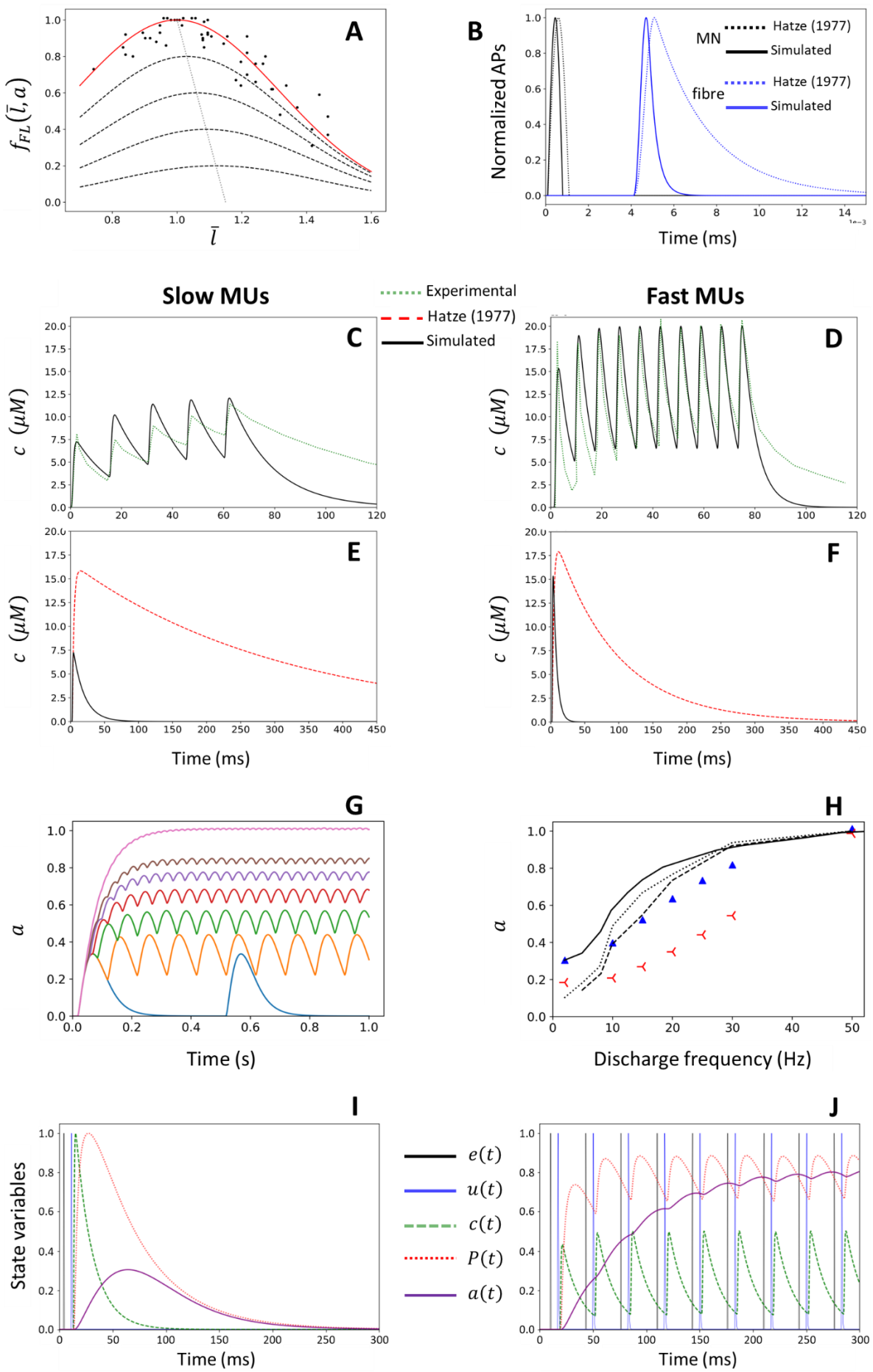
A
$f_{FL}(\bar{l}, a)$
$\bar{l}$
B
Normalized APs
MN
Hatze (1977)
Simulated
fibre
Hatze (1977)
Simulated
Time (ms)
Slow MUs
Fast MUs
Experimental
Hatze (1977)
Simulated
C
D
E
F
c (μM)
Time (ms)
G
H
a
Time (s)
Discharge frequency (Hz)
I
J
State variables
$e(t)$
$u(t)$
$c(t)$
$P(t)$
$a(t)$
Time (ms)

488

Figure 4: Contraction, Excitation, and Activation Dynamics (Figure 3) of the slow and fast MUs constituting the MN-driven neuromuscular model.
(A) Normalized FL relationship describing the scaling factor f_{FL}. The experimental data points (dots), obtained from human skinned fibres (Gollapudi & Lin, 2009), were fitted (solid red curve) with EQ. 11. f_{FL} is nonlinearly dependent on the MU active state a at submaximal levels (dashed lines) (Lloyd & Besier, 2003), where the apparent optimal MU length l_0^M increases by up to 15% (dotted line).
(B) Time-history of the MN (black curves) and fibre (blue curves) normalized APs simulated with EQ. 12 and EQ. 13, respectively. The solid lines were obtained after tuning the coefficients in those equations (Table 1) to fit cat experimental data, while the dotted lines, reported for comparison, were obtained from simulations using the original amphibian data as in Hatze's work (Hatze, 1977).
(C-F) Time-course of the free calcium concentration c in μM for slow (C, E) and fast (D, F) MUs. The calcium transients simulated after tuning the coefficients in EQ. 14 to match experimental rodent data (Table 1) are displayed with solid black lines. The simulated transients were validated against other experimental (Hollingworth, S. et al., 1996; Baylor, S. M. & Hollingworth, 2003) traces (green dotted lines) at 67Hz (C) and 125Hz (D) stimulation, respectively. In (E, F), the simulated transients were compared against those proposed in Hatze's work (Hatze, 1977) for amphibians (red dotted curves).
(G, H) Relationship between the amplitude of the simulated active state a and the MN firing frequency in Hz. (G): for slow-type MUs, time-history of the active state $a(t)$ with increasing MN firing frequency at 2 (blue), 10 (orange), 15 (green), 20 (red), 25 (purple), 30 (brown) and 50 Hz (pink) where the activation twitches fuse to reach 1.0 at steady-state. (H) Activation-Frequency relationship in the steady-state. Simulations for slow and fast-type MUs are displayed in blue triangles and red symbols respectively. Experimental torque-frequency relationships obtained from FDL(dotted trace, (Fuglevand et al., 1999)), EDB (solid trace, (Macefield et al., 1996)) and thenar (dashed trace, (Thomas, C. K. et al., 1991)) muscle fibres are superimposed.
(I, J) The bottom row displays the time-course of the five state variables describing the dynamics of the Neuromechanical Element when the MU receives a unique nerve impulse (I) and a train of nerve impulses at 30Hz (J). Black and blue solid curves: trains of MN and muscle unit action potentials $e(t)$ and $u(t)$. Green dashed curve: free calcium concentration $c(t)$. Red dotted curve: CaTn concentration $P(t)$. Purple solid curve: MU active state $a(t)$. Except for the MU active state, the quantities were normalized to their maximum physiological values for visual purposes.

5. Neural control to the MN-driven neuromuscular model

5.1. Neural controls to the neuromuscular model

In this study, we assessed the MN-driven neuromuscular model (Figure 1F) with two different types of neural controls, i.e., the experimental samples of N_r identified spike trains (Figure 1C) and the complete population of N MU spike trains (Figure 1D) obtained with a MU pool reconstruction method (Caillet et al., 2022a). Both approaches were tested with the sets of spike trains identified with the three electrode densities (Figure 1B) at both contraction intensities up to 30% and 50% MVC.

When directly inputting the N_r experimental spike trains to the neuromuscular model, the N_r MUs were assigned with EQ. 19 representative maximum isometric forces $\overline{f_{k,0}^{MU}}$, necessary parameter in EQ. 10, to account for the force-generating capacities of their neighbouring MUs, in the sense of their recruitment thresholds, that were not identified experimentally. The muscle force $F_{N_r,1}^M(t)$ (blue dotted line in Figure 1G) was first predicted when the N_r identified MUs were assumed to be homogeneously spread across the Tth-ranked MU pool, in which case the $f_0^{MU}(i)$ distribution in EQ. 8 was evenly split in N_r domains along the x-axis (Figure 2B). A second TA force $F_{N_r,2}^M(t)$ (green dashed line in Figure 1G) was predicted after assigning to the N_r MUs representative maximum forces with

EQ. 19 after a physiological mapping of these MUs to the complete T^{th}-ranked MU pool using EQ. 6. For example, when N_r = 30 MUs are identified at 30% MVC, where N_a =300 MUs are supposed to be recruited (EQ. 5), the 9th, 10th, and 11th identified MUs in the Tth-ranked experimental sample are mapped into the complete T^{th}-ranked pool to the 90th, 100th, and 110th MUs with the first method (considering even steps of $\left\lfloor \frac{N_a}{N_r} \right\rfloor = \left\lfloor \frac{300}{30} \right\rfloor = 10$ MUs) and to the 90th, 120th, and 180th MUs with the second method (using EQ. 6). The 10th identified MU represents 10 MUs and produces the combined force $f_{0,10}^{MU} = \sum_{j=96}^{105} f_0^{MU}(j) = 13$ N with the first method, while it represents 45 surrounding MUs and generates $f_{0,10}^{MU} = \sum_{j=106}^{150} f_0^{MU}(j) = 71$ N with the second method.

$$i \rightarrow N_i = \left\{ i \cdot \left\lfloor \frac{N_a}{N_r} \right\rfloor ;\ \text{or from MU mapping} \right\},\ i \in [\![1; N_r]\!], N_i \in [\![1; N]\!]$$

$$N_{i,1} = \left\lfloor \frac{N_{i-1} + N_i}{2} \right\rfloor + 1$$

$$N_{i,2} = \left\lfloor \frac{N_i + N_{i+1}}{2} \right\rfloor \qquad \text{EQ. 19}$$

$$f_{0,i}^{MU} = \sum_{j=N_{i,1}}^{N_{i,2}} f_0^{MU}(j)$$

The TA force $F_N^M(t)$ (red solid line in Figure 1G) was predicted from a comprehensive cohort of $N = 400$ simulated spike trains, that described the discharge activity of a completely reconstructed MU population (red solid line in Figure 1E). The complete population of N MUs was obtained from a validated computational method (Caillet et al., 2022a) that maps with EQ. 6 the N_r MUs into the MU pool and infers from the N_r identified spike trains a continuous distribution of the MN electrophysiological properties across the MU pool to physiologically scale a cohort of $N = 400$ models of motoneurons that predicts the discharge activity of the $N - N_r$ MUs that were not identified experimentally. The implementation of the method is publicly available at https://github.com/ArnaultCAILLET/Caillet-et-al-2022-PLOS_Comput_Biol. Here, the distribution of MU maximum forces $f_0^{MU}(i)$ in EQ. 8 was directly applied to the reconstructed population of N MUs.

5.2. Neural drive to muscle and quality of the experimental neural control

Cumulative spike trains were computed as the temporal binary summation of the pools of spike trains and were low-pass filtered in the bandwidth [0-4] Hz relevant for force generation (Negro, Yavuz et al., 2016) to approximate the effective neural drive to muscle $D(t)$. As suggested for isometric contractions (Farina & Negro, 2015), the normalized effective neural drive $\overline{D}(t)$ was compared for validation against the normalized experimental TA force $\overline{F_{TA}}(t)$ (black trace in Figure 1E) with

calculation of three metrics: the error in seconds in identifying the onset of the neural drive Δ_1, the normalized root-mean-square error (nRMSE) and the coefficient of determination r^2. Of note, $\overline{F_{TA}}(t)$ was obtained by normalization to the average of the $F_{TA}(t)$ values over the plateau of contraction and not to the maximum registered F_{TA} value to minimize the impact of possible discharge artefacts onto the interpretation of the nRMSE metric. To discuss the importance of the quality of the experimental data in deriving a reliable neural control to the MN-driven neuromuscular model developed in this study, the validation between the $\overline{D}(t)$ and $\overline{F_{TA}}(t)$ traces was performed for both the pools of N_r experimental and N reconstructed spike trains (blue dotted and plain red traces in Figure 1E, respectively) derived from the three grids of increasing electrode density (Figure 1B).

6. Validation of the predicted forces

The TA forces $F^M(t)$ predicted with the MN-driven neuromuscular model (Figure 1F) were validated against the experimental TA force $F_{TA}(t)$ (solid black trace in Figure 1G), that was estimated from the recorded ankle torques $T(t)$ with EQ. 4. The $F^M(t)$ versus $F_{TA}(t)$ validation was performed with calculation of {1} the error in seconds in identifying the onset Δ_1 of generated force, i.e. when 1% of the max generated force was produced, {2} the experimental force Δ_1^F developed after the Δ_1 delay, {3} the maximum error (ME) in Newtons, {4} the nRMSE in percentage, and {5} r^2. The nRMSE was calculated for the complete contraction, the ascending ramp ($nRMSE_{r1}$), the plateau ($nRMSE_p$), and the descending ramp ($nRMSE_{r2}$). Δ_1 and Δ_1^F assess the delay in predicting the onset of force and only depends on the first discharge time identified experimentally (Caillet et al., 2022a), ME identifies the maximum error in predicting the whole muscle force and is related to the Δ_1 and Δ_1^F metrics in the regions of low generated force, the nRMSE metric evaluates the accuracy in predicting the amplitude of the predicted whole muscle force, which mainly relies on both the distribution of MU tetanic forces and the accurate prediction of the MU active states, and r^2 evaluates the time-course of the variation of the muscle force, which mainly relies on the distribution of the MU neuromechanical properties across the MU pool.

Results

1. Subject-specific MSK quantities and experimental TA force

The subject-specific MSK model (Figure 1I) yielded the subject-muscle-specific properties in Table 2 for the TA muscle and for its agonist EDL and EHL, and antagonist muscles SOL, GM, and GL in ankle dorsiflexion. By reapplying with EQ. 4 the exponential $\Delta T(T(t))$ relationship derived from the bEMG and torque recordings obtained during the second experimental session to the torque traces $T(t)$ recorded during the first experimental session, the experimental TA force $F_{TA}(t)$ (solid red traces in Figure 5) was estimated (see Appendix A.1 for details of the calculation). In the normalized space (bottom row in Figure 5), $\overline{F_{TA}}(t)$ compared well to the muscle force that would be computed if the TA alone produced the total recorded ankle torque T (black dashed traces in Figure 5), with a maximum error ≤ 15%, nRMSE ≤ 7%, and $r^2 \geq 0.98$. Yet, ignoring the co-contracting activities of the EDL, EHL, SOL, GM, and GL muscles would underestimate the TA force F_{TA} by up to 49 N and 283 N, i.e., 18% and 60% of the maximum F_{TA} value, at 30% and 50% MVC respectively (upper row in Figure 5).

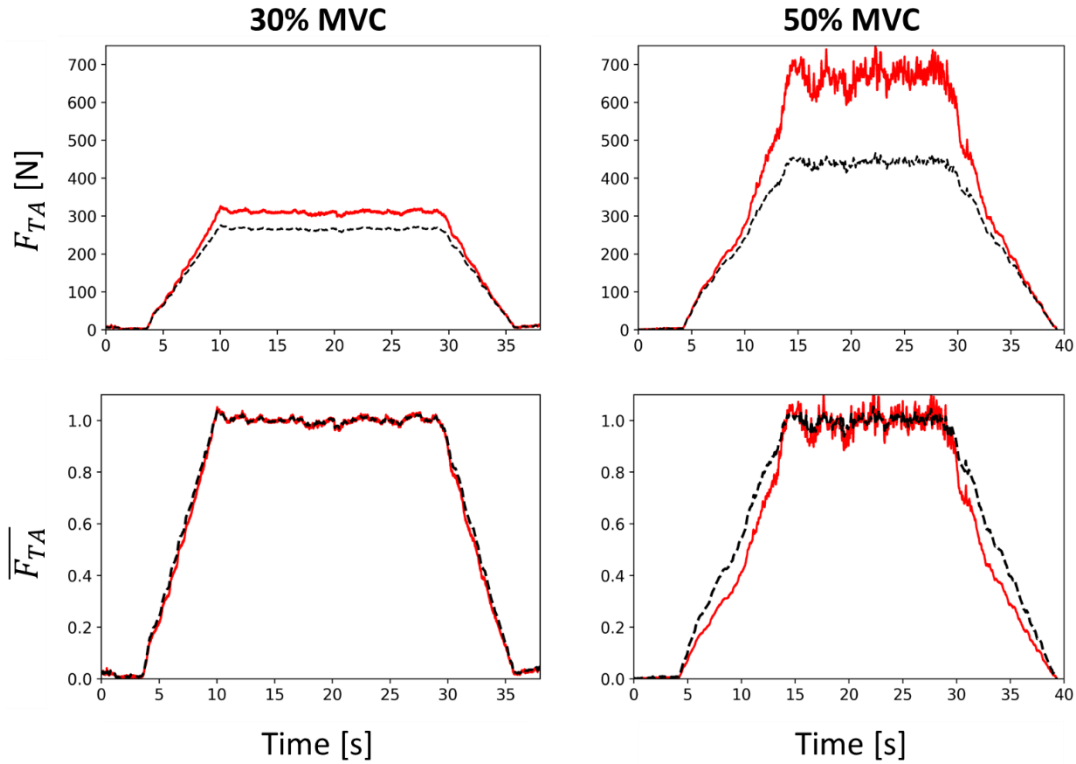

Figure 5: Estimation of the force developed by the TA muscle during the trapezoidal dorsiflexions up to 30% (left) and 50% MVC (right) performed during the first experimental session. The TA forces (first row: in Newtons, second row: normalized), displayed in solid red traces, were estimated by correcting the recorded torque T for co-contraction with the relationship in EQ. 4 (See Appendix A.1 for details about the calculation). The black dashed traces display the TA force calculated without considering the co-contraction of surrounding muscles (as if the TA alone produced the entire recorded ankle torque T).

Table 2: Summary of the subject-muscle-specific MSK properties of the six flexor muscles when the ankle joint is set to a 30° plantarflexion angle. The moment arm L made by the tendons with the ankle joint and the muscle-

tendon lengths l^{MT} were identified by MRI segmentation and measurements in NMSBuilder (Valente et al., 2017) and OpenSim (Delp et al., 2007; Seth et al., 2018). The optimal length l_0^M and the tendon slack length l_s^T were scaled from the generic values reported in Rajagopal et al. (2016) with the ratio of generic to subject-specific muscle-tendon lengths l^{MT} at default 0° plantarflexion angle. The muscle maximum isometric force F_0^M was estimated from the muscle volume V^M, which was obtained from MRI segmentation for the TA, and from anatomical relationships (Handsfield et al., 2014) for the other muscles. The normalized muscle lengths $\bar{l}$, at 30° angle in ankle plantarflexion and assuming a rigid tendon, were calculated with EQ. 20 in Appendix A.1.

Muscle	$L\ [mm]$	$F_0^M [N]$	$l^{MT} [mm]$	$l_0^M [mm]$	$l_s^T [mm]$	$\bar{l}$
TA	25.5	1046	319	67.6	239	1.18
EDL	26.1	403	525	80.5	462	0.78
EHL	25.9	176	487	87.6	382	1.20
SOL	51.1	3822	373	54.1	340	0.60
GM	51.8	2232	447	52.6	411	0.68
GL	52.2	1058	448	62.4	398	0.80

2. Experimental neural control

For the contractions up to 30% and 50% MVC, 81, 32, and 14 MUs, and 55, 15, and 3 MUs (Figure 1C) were respectively identified (Caillet et al., 2023) with the EMG grids of 4, 8, and 12 mm interelectrode distance (Figure 1B). The dataset of three identified MUs was disregarded in the following results because it provided a highly inaccurate description of the discharge activity of the real MU pool. The histogram distribution of those identified MUs across the MU pool according to their recruitment threshold T^{th} in %MVC is displayed in Figure 6. Importantly, the denser the EMG grid and the lower the generated force, the more homogeneous the distribution of the identified MUs across the MU pool (Caillet et al., 2023). For example, 12% to 20% of the MUs decoded with the densest grid at 30% MVC were systematically identified in each of the 5% ranges sampling the recruitment range (histogram in Figure 6C). The normalized effective neural drive to muscle $\bar{D}(t)$ (Figure 1E) was computed with these cohorts of spike trains and was validated against the experimental normalized TA force $\overline{F_{TA}}(t)$ (black solid traces in Figure 6) with the three validation metrics reported in Table 3.

The normalized effective neural drive $\bar{D}(t)$ estimated from the experimental samples of N_r MUs (blue dotted lines in Figure 6) was always better approximated when the electrode density increased, especially in the regions of low generated forces. For example, at 30% MVC, it was obtained $\Delta_1 = 0.07\ s$, $nRMSE = 8.0\ \%$, and $r^2 = 0.97$ from the 81 discharging MUs identified with 4 mm interelectrode distance, while the 14 MUs identified with 12 mm interelectrode distance returned $\Delta_1 = 0.14\ s$, $nRMSE = 17.5\ \%$, and $r^2 = 0.89$ (Table 3). The effective neural drive $\bar{D}(t)$ estimated from the experimental MU samples was always better approximated at 30% MVC than at 50% MVC

(blue dotted traces in upper row versus lower row in Figure 6), with two to three times lower nRMSE values, and strongly lower Δ_1 and higher r^2 values, respectively (Table 3).

Complete populations of $N = 400$ MNs (Figure 1D) were also reconstructed from the discharge activity of the N_r identified MNs by estimating the discharge activity of the MUs not identified experimentally (Caillet et al., 2022a). In this case, the $\overline{D}(t)$ estimated at 30% MVC (solid red lines, upper row, in Figure 6) was accurately predicted and was unrelated to the quality of the input experimental samples, with $nRMSE < 7\%$, and $r^2 = 0.98$ for the three EMG grid configurations (Table 3). At 50% MVC, the $\overline{D}(t)$ derived from the N MNs (solid red lines, bottom row, in Figure 6) was better estimated when the MU pool was reconstructed from denser grids of electrodes, with lower nRMSE and higher r^2 values (Table 3). As for the experimental MU samples, $\overline{D}(t)$ estimated from the $N = 400$ MUs was better approximated at 30% MVC than at 50% MVC (solid red traces in upper row versus lower row in Figure 6). At 50% MVC, the reconstructed populations of discharging MUs returned inaccurate estimations of the onset and ascending ramp of force, with $\Delta_1 > 1s$, $nRMSE > 12\%$, and $r^2 \leq 0.95$. Overall, the normalized effective neural drive $\overline{D}(t)$ was systematically better approximated by the reconstructed pool of $N = 400$ MUs than by the experimental samples of N_r identified MUs (solid red versus blue dotted traces in Figure 6) with lower nRMSE and higher r^2 values (Table 3).

Therefore, $\overline{D}(t)$ was best approximated by samples of MU spike trains of identified MUs that spanned across the whole recruitment range and followed a homogeneous distribution across the MU pool. Obtaining such representative description of the discharge behaviour of the real MU pool was possible with EMG signals recorded at 30% MVC with high electrode density (4 mm interelectrode distance) or, to some extent, with the computational reconstruction of the complete MU pool, both of which aimed to correct for the systematic bias of HDEMG decomposition towards identifying the higher-threshold MUs (histograms in Figure 6) of the discharging MU pool (Caillet et al., 2023).

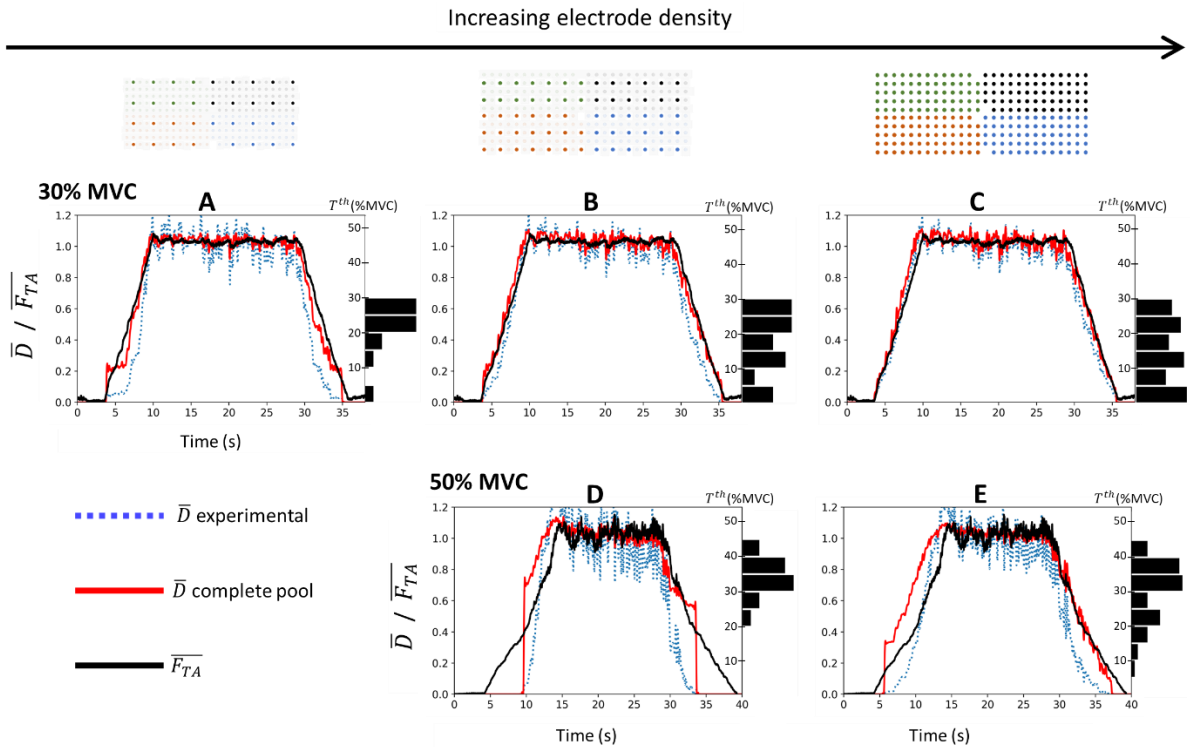

Figure 6: For the three grid configurations of increasing electrode density (in columns) and for both contractions up to 30% MVC (first row) and 50% MVC (second row), validation against the experimental normalized force trace $\overline{F_{TA}}(t)$ (solid dark trace) of the normalized effective neural drive to muscle $\overline{D}(t)$ estimated from the completely reconstructed population of $N = 400$ MUs (solid red traces) and from the experimental samples of N_r identified MUs (dotted blue traces). The TA force $F_{TA}(t)$ (Figure 5) was estimated from the recorded ankle torque T with EQ. 4. The histogram distributions of the identified MUs across the recruitment range T^{th} in %MVC were normalized to the number of MUs identified experimentally.

Table 3: Validation of the normalized effective neural drive to muscle $\overline{D}(t)$ for both contractions up to 30% and 50% MVC, computed from the spike trains obtained with the three grid configurations of 4, 8, and 12 mm interelectrode distance that involve 256, 64, and 36 EMG electrodes respectively. The validation was performed for both the experimental samples of N_r identified MUs, and for the completely reconstructed pool of N MUs.

			N_r MNs (experimental)		N MNs (simulated)	
Contraction	**Electrode density (mm)**	Δ_1 (s)	$nRMSE$ (%)	r^2	$nRMSE$ (%)	r^2
30% MVC	**4**	0.1	8.0	0.97	5.3	0.98
	8	0.1	10.5	0.95	5.3	0.98
	12	0.1	17.5	0.89	6.3	0.9
50% MVC	**4**	1.2	16.4	0.87	12.9	0.95
	8	5.2	24.2	0.77	16.4	0.89

Activation and Contraction dynamics of the MU pool and TA Force validation

The neuromuscular model was built as populations of N_r or N in-parallel FGs, whether it received as neural control the experimental samples of N_r identified spike trains (Figure 1C) or the completely reconstructed populations of N MU spike trains (Figure 1D). According to Figure 2, around 298 and 355 MUs were recruited over the trapezoidal contractions up to 30% and 50% MVC, respectively, in which case all the modelled discharging MUs were assigned slow-type properties for their activation dynamics (Figure 3).

Figure 7A displays the distribution of the maximum values of the modelled MUs' activation states over the contraction up to 30% MVC, that were estimated from the cohorts of $N_r = 81$ (green triangles) and $N = 400$ (red dots) spike trains with EQ. 12 to EQ. 18. Consistent with the onion skin theory (De Luca & Hostage, 2010) where MN discharge rate and recruitment threshold are negatively related, the estimated MU activation was overall negatively related to recruitment threshold, with low-threshold MUs reaching maximum activation states up to $a = 0.80$ and higher-threshold MUs as low as $a = 0.18$. Because of trendline fitting during the reconstruction process of the MU pool (Caillet et al., 2022a), the monotonically decreasing distribution of active states of the N-population did not account for the physiological variability in MN discharge rate with recruitment threshold (green triangles in Figure 7A). The same conclusions were obtained with the neural controls obtained with the grids of lower EMG electrode densities and at 50% MVC.

Figure 7B-D displays the distribution of the maximum forces (blue crosses, green triangles, red dots) developed by the modelled MUs over the contraction up to 30% MVC, that were estimated with EQ. 10 from the MUs' active states $a(t)$, the common MU length $\bar{l}$, and the MU-specific maximum isometric forces $f_{k,0}^{MU}$ (black dots), for cohorts of $N_r = 81$ (Figure 7B, C) and $N = 400$ (Figure 7D) MUs. Depending on the modelling approach, the modelled MUs were assigned maximum MU forces $f_{k,0}^{MU}$ (black dots in Figure 7B-D) by either blindly assuming the N_r MUs to be evenly distributed across the MU pool (Figure 7B), mapping the N_r MUs to the real MU pool with EQ. 6 (Figure 7C), or directly applying the $f_0^{MU}(k)$ distribution in EQ. 8 to the complete MU pool (Figure 7D). Depending on the approach, the individual MUs produced maximum forces f_k^{MU} over the contraction up to 30% MVC in the range 1.8-6.6 N, 0.4-16.5 N, and 0.5-1.5N (blue crosses in Figure 7B, green triangles in Figure 7C, and red dots in Figure 7D, respectively), and in the range 4.2-16.2 N, 1.5-136.7 N, and 0.7-2.2 N at 50% MVC. Only the reconstructed pool of $N = 400$ MUs (Figure 7Figure 8D) provided a window onto the continuous distribution of the dynamics of the MU pool with physiological generated MU forces.

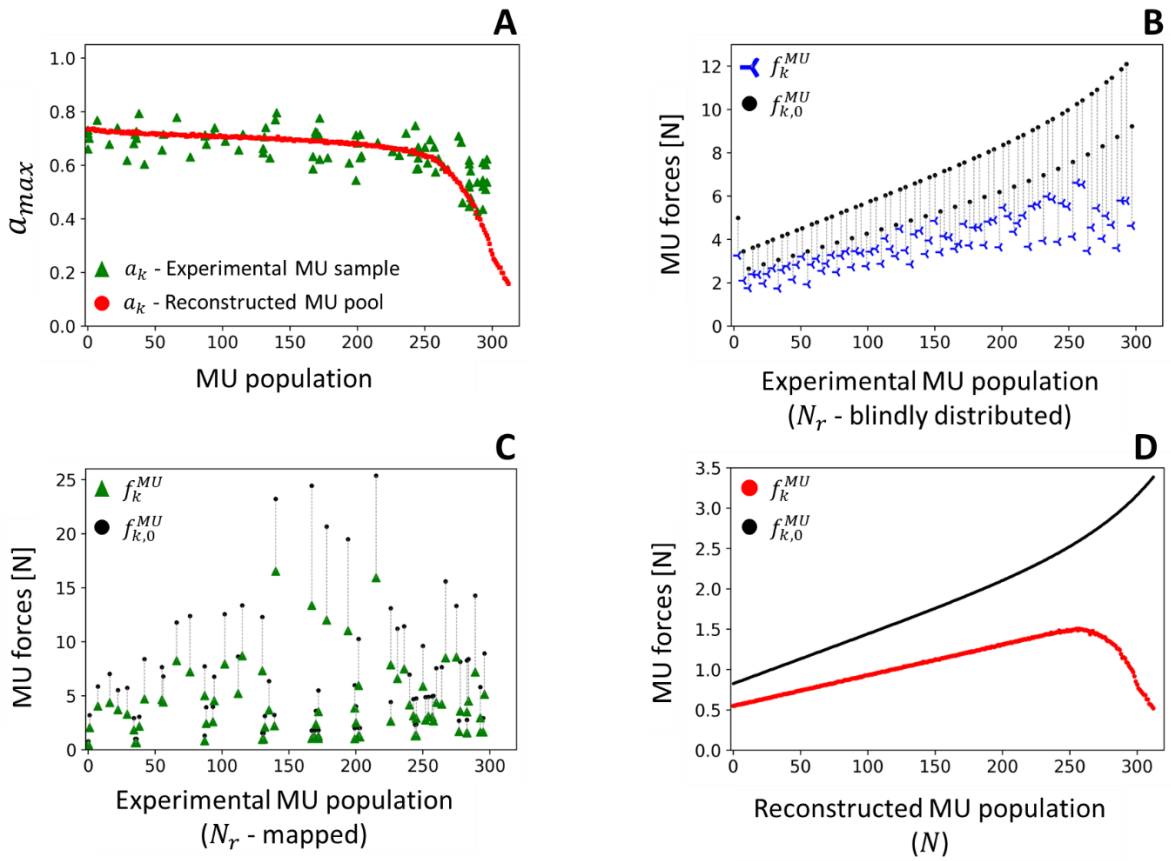

Figure 7: Distribution across the Tth-ranked MU population of the maximum values at 30% MVC of the MU activation states a_k (A) and MU forces f_k^{MU} (B-D) simulated with the MN-driven neuromuscular model. The model either received as neural input the $N_r = 81$ experimental spike trains (green triangles in A for a_k; plots B and C for f_k^{MU}) or the discharge activity of the complete pool of $N = 400$ MUs (red dots in A for a_k; plot D for f_k^{MU}). In B-D, the black dots represent the distribution of the MUs' maximum forces $f_{k,0}^{MU}$, which is continuous for the completely reconstructed pool (D). In B and C, the N_r identified MUs were assigned representative maximum forces $f_{k,0}^{MU}$ (black dots) to account for the force-generating properties of the MUs not identified experimentally. To do so, in B, the N_r identified MUs were assumed to be homogeneously distributed across the Tth-ranked MU pool, while they were accurately mapped to the real pool with EQ. 6 in C. In B, the non-continuous distribution of the $f_{k,0}^{MU}$ values is explained by the fact that $\frac{N}{N_r}$ is not an integer value in EQ. 19.

The simulated MU forces were processed and linearly summed with EQ. 10 to yield the three predicted whole muscle forces in Figure 8A-E $F_{N_r,1}^M(t)$ (experimental MU population with blind $f_{k,0}^{MU}$ distribution - blue dotted traces), $F_{N_r,2}^M(t)$ (experimental MU population with MU mapping - green dashed traces), and $F_N^M(t)$ (reconstructed MU population - solid red traces), which were validated against the experimental TA force $F_{TA}(t)$ (solid black traces) with the validation metrics in Table 4.

When high numbers of MUs were homogeneously identified over the full range or recruitment ($N_r = 81$ MUs, 30% MVC, 4 mm interelectrode distance), i.e., when $\overline{D}(t)$ was accurately estimated from the experimental samples of spike trains (Figure 6C), F_{TA} was predicted by $F_{N_r,1}^M$, $F_{N_r,2}^M$, and F_N^M with the

same level of accuracy (Figure 8C) for the eight validation metrics in Table 4 with $r^2 \geq 0.98$, all $nRMSE$ values below 10%, and ME in 36-66 %, irrespective from the three choices of $f_{0,k}^{MU}$ assignment (black dots in Figure 7B-D).

In all other cases, $F_{TA}(t)$ was the most accurately predicted by both $F_N^M(t)$ when the complete MU pool was modelled (solid red traces in Figure 8A-E, $nRMSE$ in range 7-13% and r^2 in range 0.97-0.99 at 30% MVC, and $nRMSE$ in range 15-16% and r^2 in range 0.90-0.95 at 50% MVC) and $F_{N_r,2}^M(t)$ when the population sample of N_r MUs was assigned representative $f_{0,k}^{MU}$ values according to a MU mapping (green dashed traces in Figure 8A-E, $nRMSE$ in 6-11% and r^2 in 0.97-0.99 at 30% MVC, and $nRMSE$ in 14-20% and r^2 in 0.92-0.95 at 50% MVC). The least accurate predictions were systematically obtained with $F_{N_r,1}^M(t)$ when the population sample of N_r MUs received experimental neural inputs and was blindly assigned $f_{0,k}^{MU}$ values (blue dotted traces in Figure 8A-E, $nRMSE$ in 7-19% and r^2 in 0.89-0.98 at 30% MVC, and $nRMSE$ in 27-32% and r^2 in 0.86-0.92 at 50% MVC). $F_N^M(t)$ and $F_{N_r,2}^M(t)$ performed better than by $F_{N_r,1}^M(t)$ especially over the ramps of force with around 1.5-3 times lower ME, $nRMSE_{r1}$, and $nRMSE_{r2}$ values ($nRMSE_{r1}$ and $nRMSE_{r2}$ metrics calculated over the ramps of force - Table 4), because the blind distribution of f_0^{MU} values in $F_{N_r,1}^M$ (Figure 7B) did not correct, contrary to the two other approaches, for the experimental bias towards identifying relatively more high-threshold MUs with decomposed HDEMG signals and overestimated their force-generating activities in the MU pool. As long as the N_r decoded MUs were homogeneously spread across the identified portion of the MU pool, $F_{N_r,2}^M$ returned slightly more accurate predictions of F_{TA} than F_N^M, with slightly lower *nRMSE* and *ME* values over the whole contraction. Mainly, F_N^M returned higher $nRMSE_p$ values (Table 4) calculated over the plateau of force because of the noisy force-generating activity of the highest-threshold recruited MUs modelled with the reconstruction method (Caillet et al., 2022a). With experimental samples of lesser quality (50% MVC, 8 mm interelectrode distance, Figure 6), F_N^M performed better than $F_{N_r,2}^M$.

For all three modelling approaches at both contraction levels, F_{TA} was more accurately predicted according to all the validation metrics when the electrode density increased, especially during the ramps of force. For example, at 30% MVC, it was obtained $\Delta_1 = 0.1\ s$, $\Delta_1^{\mathrm{F}} = 16\ N$, $nRMSE$ in 6-8%, and r^2 in 0.98-0.99 from the 81 discharging MUs identified with 4 mm interelectrode distance, while the 14 MUs identified with 16 mm interelectrode distance returned $\Delta_1 = 0.2\ s$, $\Delta_1^{\mathrm{F}} = 29\ N$, $nRMSE$ in 11-19%, and r^2 in 0.89-0.98 (Table 4).

As expected from the neural drive estimation in Figure 6, for all the modelling approaches and EMG grid configurations, F_{TA} was more accurately predicted at 30% MVC than at 50% MVC (upper row

versus lower row in Figure 6), with two to three times lower *nRMSE* values, and strongly lower Δ_1 and Δ_1^{F} and higher r^2 values, respectively (Table 4).

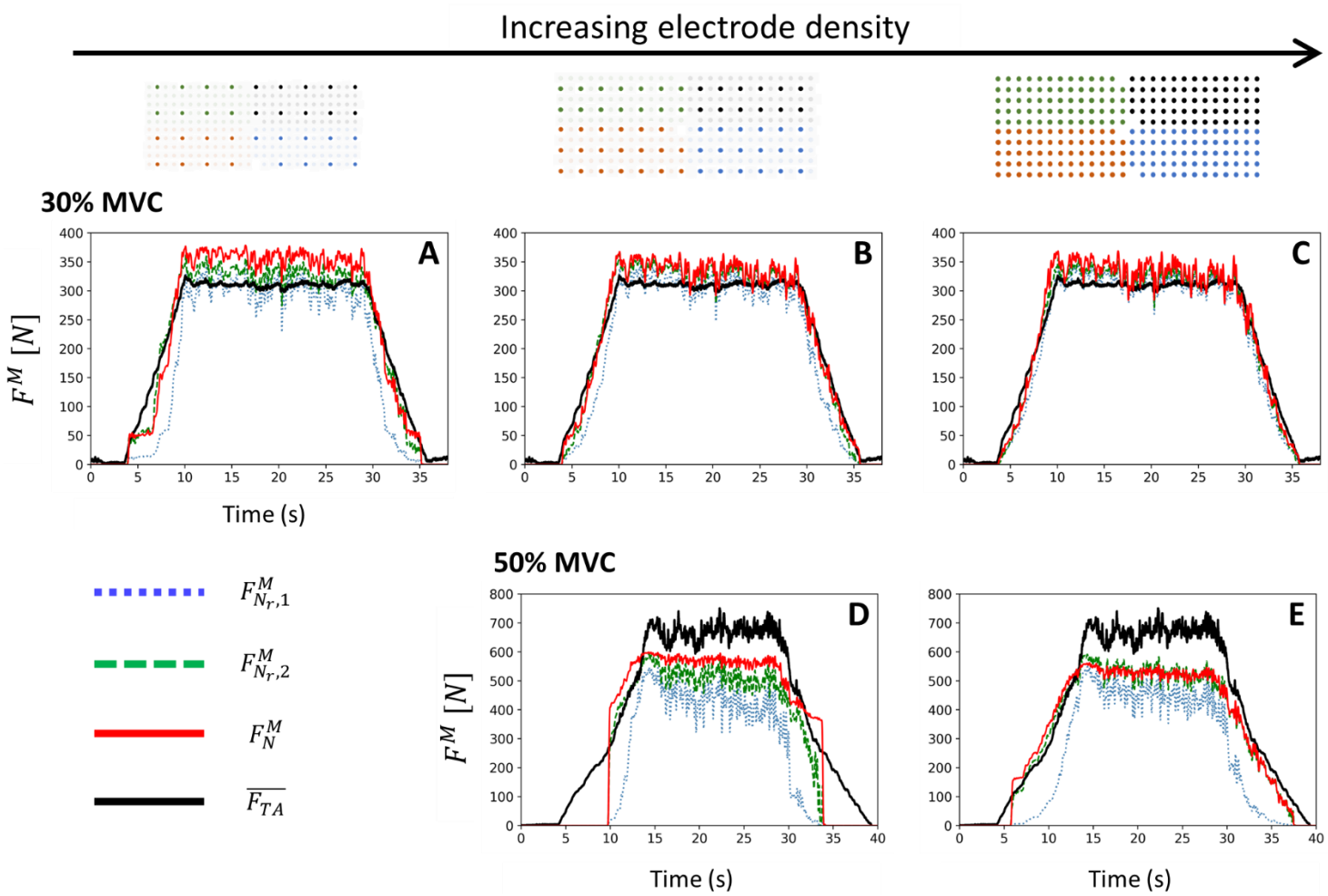

Figure 8: For the three grid configurations of increasing electrode density (in columns) and for both contractions up to 30% MVC (first row) and 50% MVC (second row), validation against the experimental force trace $F_{TA}(t)$ (solid dark trace) of the TA force $F^M(t)$ estimated with the MN-driven neuromuscular model in Figure 1F. $F^M(t)$ was estimated from the completely reconstructed population of $N = 400$ MUs ($F^M_N(t)$, solid red traces) and from the experimental samples of N_r identified MUs when 'blind' ($F^M_{N_r,1}(t)$, blue dotted traces) and T^{th}-informed ($F^M_{N_r,2}(t)$, green dashed traces) distributions of the MU maximum isometric forces $f_0^{MU}(i)$ were assigned to the MU samples. The experimental TA force $F_{TA}(t)$ was estimated from the recorded ankle torque T with EQ. 4.

Table 4: Validation against the experimental force trace $F_{TA}(t)$ of the predicted TA force $F^M(t)$ at 30% and 50% MVC. $F^M(t)$ was predicted from the spike trains obtained at 4-, 8-, and 12-mm electrode density. $F^M(t)$ was estimated from the completely reconstructed population of $N = 400$ MUs (F_N^M) and from the experimental samples of N_r identified MUs when 'blind' ($F_{N_r,1}^M$) and T^{th}-informed ($F_{N_r,2}^M$) distributions of the MU maximum isometric forces $f_0^{MU}(i)$ were assigned to the MU samples. $nRMSE, nRMSE_{r1}, nRMSE_p, nRMSE_{r2}$ were calculated for the whole contraction, and over the ascending ramp, plateau, and descending ramp, respectively.

Contraction	Electrode density (mm)	Validated Forces $\boldsymbol{F^M(t)}$	$\boldsymbol{\Delta_1}$ $(\boldsymbol{s})$	$\boldsymbol{\Delta_1^F}$ $(\boldsymbol{N})$	$\boldsymbol{ME}$ (N)	$\boldsymbol{nRMSE}$ (%)	$\boldsymbol{nRMSE_{r1}}$ (%)	$\boldsymbol{nRMSE_p}$ (%)	$\boldsymbol{nRMSE_{r2}}$ (%)	$\boldsymbol{r^2}$
30% MVC	**4**	$F_{N_r,1}^M$	0.1	16	56	7	9	5	10	0.98
		$F_{N_r,2}^M$	0.1	16	36	6	6	6	6	0.99
		F_N^M	0.1	16	66	8	6	9	4	0.99
	8	$F_{N_r,1}^M$	0.2	29	81	11	15	5	16	0.96
		$F_{N_r,2}^M$	0.2	29	44	7	7	7	6	0.99
		F_N^M	0.2	29	55	8	5	9	4	0.99
	12	$F_{N_r,1}^M$	0.2	29	159	19	26	6	25	0.89
		$F_{N_r,2}^M$	0.2	29	82	11	9	7	8	0.97
		F_N^M	0.2	29	87	13	11	15	8	0.97
50% MVC	**4**	$F_{N_r,1}^M$	2.9	157	333	27	19	33	28	0.92
		$F_{N_r,2}^M$	1.5	100	242	14	4	21	8	0.96
		F_N^M	1.5	100	215	15	6	22	8	0.95
	8	$F_{N_r,1}^M$	5.6	268	412	32	24	36	34	0.86
		$F_{N_r,2}^M$	5.4	262	286	20	16	24	19	0.92
		F_N^M	5.5	268	255	16	17	15	17	0.9

Discussion

Summary of the work

This study reports a novel approach, summarized in Figure 1, to develop a MN-driven neuromuscular model, that is controlled at the level of the individual MU with experimental motoneuronal data. This model advances the recently reviewed (Caillet et al., 2022c) state-of-the-art of neuromuscular modelling on multiple aspects, and finds applications in the complementary fields of motor control and MSK modelling, including human-machine interfacing (Farina et al., 2017; Farina et al., 2021). The population of Hill-type MU actuators (Figure 1F) transform, with advanced models of the MU's excitation, activation, and contraction dynamics (Figure 3, Figure 4), a vector of MN spike trains into a vector of transient MU forces that sum across the modelled MU population to yield the whole muscle force (Figure 8). The neuromuscular model and the continuous distribution of the MU's recruitment and force-generating properties across the MU pool were respectively made subject-specific using a subject-specific MSK model derived from medical images (Figure 1H, I), and muscle-specific, using results from the literature (Figure 2). The neural control to the MN-driven model is also subject-specific as the vector of input MN spike trains is derived from HDEMG signals recorded during the participant's voluntary task (Figure 1A, B). The experimental vector of N_r identified spike trains resulting from HDEMG signal processing was either directly input to the neuromuscular model of N_r MUs (Figure 1C) or first extrapolated to an estimation of the discharge activity of the complete population of N MNs (Caillet et al., 2022a), which was then input to the neuromuscular model of N MUs (Figure 1D). The accuracy in estimating the neural drive to muscle of this novel MN-driven approach was assessed using experimental datasets of varying quality (Figure 6), with the control vectors of N_r and N MN spike trains (Figure 1E). Finally, the whole muscle force predicted by the MN-driven neuromuscular model was validated against an experimental muscle force (Figure 1G, Figure 8), that was estimated from measured joint torque and bEMG signals recorded from agonist and antagonist muscles (Figure 1J, Figure 5).

Relevance for the field of neuromuscular modelling

The neuromuscular model developed in this study was built as a collection of in-parallel MU actuators, which proved beneficial for advancing the recently reviewed (Caillet et al., 2022c) state-of-the-art of neuromuscular modelling on several aspects.

For the first time in Hill-type modelling, we controlled the individual MUs of a modelled MU population with a vector of dedicated experimental motoneuronal controls. The vector of MN spike trains obtained from HDEMG signals provided a comprehensive description of both the dynamics of MU recruitment and MU rate coding for the modelled population of MUs. Conversely in EMG-driven

models of whole muscle actuators, the recruitment and discharge dynamics of the MU pool are lumped into a single phenomenological macroscopic neural control where they become indistinguishable, that is either obtained from bEMG envelopes (Hof & Van den Berg, 1981; Zajac Felix, 1989; Lloyd & Besier, 2003) or from the temporal summation of filtered cumulative spike trains and signal residuals from HDEMG signals (Sartori et al., 2017; Thompson et al., 2018; Kapelner et al., 2020). In multiscale models of single representative MUs, the dynamics of MU recruitment were either overlooked or accounted for with phenomenological models (Hatze, 1977; Hatze, 1980; Dorgan & O'Malley, 1997; Song et al., 2008; Dick, Taylor J. M. et al., 2017; Hussein et al., 2021). A few studies also assigned motoneuronal controls to modelled populations of MUs (Hatze, 1980; Legreneur et al., 1996; Callahan et al., 2013; Hamouda et al., 2016; Raikova et al., 2018; Carriou et al., 2019) but used synthetic data and/or phenomenological models, such as Fuglevand's formalism (Fuglevand et al., 1993), to describe the discharge and recruitment dynamics of the MU pool. Consequently, these models of MU populations were not used in conditions of voluntary muscle contraction and the force they predicted was indirectly validated against results from other models and not against synchronously recorded experimental data like performed in this study. A recent study (Gogeascoechea et al., 2021) implemented a neuromechanical model of a population of twitch-type models of MUs controlled by experimental vectors of MU spike trains. However, this approach was tested with limited samples of few experimental MN spike trains which are typically not representative of the true neural drive to muscle (Figure 6), twitch-type models cannot describe the interplay between the activation and contraction dynamics of the active muscle tissue as they do not rely on a description of its excitation-contraction properties like Hill-type models (Caillet et al., 2022c), and the differentiation proposed in this study of the twitch contraction time and of the MU types into bimodal distributions remains unproven in human muscles with contradictory findings (Milner-Brown et al., 1973; Thomas, Christine K. et al., 1986; Andreassen & Arendt-Nielsen, 1987; Elek et al., 1992; Cutsem et al., 1997), as reviewed (Bigland-Ritchie et al., 1998) and discussed (Caillet et al., 2022b) previously. For these reasons, the MN-driven approach developed in this study is the first that can control with experimental vectors of inputs, that are representative of the true neural to muscle, the individual MUs of a MU population in the forward prediction of human voluntary muscle contraction, while also relying on a detailed description of the excitation-contraction dynamics of the active muscle tissue and on a set of experimental spike trains that is more easily interpretable than the phenomenological neural controls used in single-input multiscale models of whole muscle actuators in the literature.

Discretely sampling the active muscle tissue into individual MUs provided a convenient framework for the precise distribution of the muscle's properties across the MU pool, including the novel experimental distributions in Figure 2 of MU recruitment threshold, maximum isometric forces, and type, some of which were never included in neuromuscular models. This description of the muscle as

845 a cohort of MUs also provided a convenient structure for deriving physiological assumptions and
846 simplifications to the rheological structure of the model (Appendix A.2) and opens avenues to
847 accounting for the impact of the muscle's internal architecture on its force-generating capacities,
848 especially if the neural control is mapped to an appropriately discretised anatomical model (Modenese
849 & Kohout, 2020). This approach has only rarely been modelled in Hill-type muscle modelling (Hatze,
850 1980; Woittiez et al., 1984; Kaufman et al., 1991).
851 This MU-scale approach was ideal for developing advanced models of the MU's excitation, activation,
852 and contraction dynamics (Figure 4). Experimental data from the literature was used in this study to
853 derive adequate mathematical equations (EQ. 11 to EQ. 18), tune physiological parameters (Table 1),
854 and validate the modelled dynamics (Figure 4). Importantly, the calibration of the parameters in EQ.
855 11 to EQ. 18 and the validation of those mathematical descriptions were performed using different
856 sets of experimental data from the literature that were measured at different discharge rates (see
857 Appendices A.3 and A.4 for details). Furthermore, we limited the amount of multiscale and inter-
858 species scaling inaccuracy, which is an important limitation of single-actuator Hill-type models (Caillet
859 et al., 2022c), by considering source experimental data, in turn and decreasing order of preference,
860 from studies on individual human MUs or bundles of fibres, human fibres and sarcomeres, cat fibres,
861 rodent fibres, rodent muscles, and amphibian fibres or muscles. In doing so, the simulated MN APs,
862 fibre APs, and free calcium twitches were more physiological and consistent with mammalian dynamics
863 than previous approaches based on experimental amphibian data at low temperature (Figure 4B, E,
864 and F). For the first time in Hill-type-like modelling, the dynamics of calcium-troponin concentration in
865 the sarcoplasm were described according to experimental data (EQ. 17) (see Appendix A.4 for details)
866 and the free calcium transients were made nonlinearly dependent to both MU length and MU type
867 based on experimental measurements (EQ. 14 to EQ. 16). Hence, this model further reconciled the
868 phenomenological Hill-type modelling approach with the real physiological mechanisms responsible
869 for muscle force generation it describes. Consequently, the completely reconstructed model of N MUs
870 provided a credible window onto the distribution of the MU's excitation-contraction dynamics across
871 the MU pool (Figure 4) that cannot be measured in human *in vivo* and suggests that at 30% MVC, for
872 example, the highest-threshold recruited MUs with the largest force-generating capacities are not
873 those producing the highest forces within the recruited pool due to low activation states explained by
874 the onion skin theory (Figure 8A, D).
875
876 <u>Experimental neural control and prediction accuracy</u>
877 The accuracy of the whole muscle force predictions in Figure 8 was mainly related to the accuracy of
878 the experimental neural control in approximating the neural drive to muscle (Figure 6). It is currently

879 impossible to identify the discharge activity of the complete MU pool of a muscle with surface EMG
880 because of the filtering effect of the volume conductor. It is however possible to increase both the
881 number of identified MUs and the ratio of identified low-threshold MUs by increasing the size and the
882 electrode density of HDEMG surface grids to obtain experimental samples of identified MUs that are
883 representative of the discharge activity of the complete MU pool (Caillet et al., 2023).

884 The experimental sample of $N_r = 81$ MUs, that was obtained at 30% MVC with a dense and large grid
885 of 256 electrodes with 4 mm interelectrode distance, was representative of the discharge activity of
886 the complete MU pool because the identified MUs both spanned across the entire recruitment range,
887 with the lowest-threshold identified MU recruited at 0.6% MVC, and were homogeneously distributed
888 across the recruited MU pool, with 12% to 20% of the identified MUs in each of the 5% ranges sampling
889 the recruitment range, as displayed with the histogram in Figure 6C. Consequently, the neural drive to
890 muscle was accurately estimated with the discharge activity of the $N_r = 81$ MUs (Figure 6C, Table 3),
891 which produced the most accurate force estimations in this study when input to the neuromuscular
892 model (Figure 8C, Table 4). Consistent with previous conclusions (Caillet et al., 2023), the experimental
893 samples obtained at 30% MVC with lower electrode density (8 and 12 mm interelectrode distance)
894 provided a less accurate description of the discharge activity of the complete MU pool. Although they
895 also spanned across the entire recruitment range, fewer MUs were identified and their distribution
896 across the MU pool shifted towards relatively larger sub-population of high-threshold MUs (histograms
897 in Figure 6A, B). Consequently, the neural drive to muscle (Figure 6A, B, Table 3) and the predicted
898 muscle force (Figure 8A and B, higher $nRMSE_{r1}$ and $nRMSE_{r2}$ values in Table 4) were underestimated
899 in the regions of low-force generation when low-threshold MUs are recruited. This experimental
900 under-representativity of the low-threshold MUs was corrected using a computational method (Caillet
901 et al., 2022a) by deriving the continuous distribution of the MN's electrophysiological properties across
902 the entire MN pool and reconstructing the discharge activity of the MUs that were not identified
903 experimentally (Figure 1D). The reconstruction method populated the two experimental samples with
904 simulated populations of low-threshold MUs, in which case the accuracy in predicting both the neural
905 drive (blue dotted versus solid red traces in Figure 6A, B) and the muscle force (Figure 8A, B)
906 systematically increased (Table 3, Table 4). As expected, this reconstruction step did not improve the
907 accuracy of the predictions for the experimental sample of $N_r = 81$ MUs, which was already
908 representative of the discharge activity of the MU pool.

909 Because of physiological reasons discussed elsewhere (Caillet et al., 2023), the discharge activity of the
910 low-threshold MUs was not identified during high-force contractions up to 50% MVC, even with high
911 electrode density. Beyond shifting the MU identification towards the highest-threshold MUs and
912 yielding imbalanced MU distributions (histograms in Figure 6D, E), the experimental samples of

identified MUs at 50% MVC did not span across the entire recruitment range, the identified MUs being first recruited above 5% and 20% MVC. Consequently, those experimental samples inaccurately predicted the onsets of the neural drive (Figure 6D, E) and of the whole muscle (Figure 8D, E) with 1.2 to 5.2 seconds delay and initial underestimations of the muscle force up to 268 N (Δ_1 and Δ_1^{F} in Table 4). Because the reconstruction method relies on the neural drive estimated from the experimental sample (Figure 6D, E), it could not correct for this source of inaccuracy (solid red traces in Figure 6 and Figure 8), although it improved the predictions by better distributing the MU's discharge activity across the identified MU pool, as discussed. It is worth noting that low-threshold MUs are usually not identified with grids of low electrode density at 30% MVC either, as hinted with the histograms in Figure 6A, B, and the resulting experimental samples of MUs hence identified usually do not span across the entire recruitment range, yielding similar prediction inaccuracies. To address this limitation when controlling single whole muscle actuators with HDEMG signals, previous studies (Sartori et al., 2017; Thompson et al., 2018; Kapelner et al., 2020) summed the experimental cumulative spike train with the EMG signal residual that was not explained by the identified MU spike trains to approximate the neural control to muscle. Consequently, the accuracy of the predictions made by the neuromuscular model developed in this study are sensitive to the number, the span, and the distribution across the MU pool of the experimental sample of identified MUs, which can, to some extent, be extrapolated to the discharge activity of the complete MU pool using our published reconstruction method (Caillet et al., 2022a).

As displayed in Figure 8A-E, the accuracy of the predicted forces $F^M(t)$ also depended on the assignment of the maximum MU isometric forces $f_{0,k}^{MU}$ to the modelled MU pool. The $f_{0,k}^{MU}$ values were obtained from the muscle-specific $f_0^{MU}(k)$ distribution in EQ. 8, which was directly mapped to the N modelled MUs when the complete MU pool was reconstructed. This physiological approach implemented the continuous distribution of the MU forces across the MU pool (Figure 7D) and almost systematically returned the most accurate $F^M(t)$ predictions (Figure 8A-E, Table 4). When the muscle was described as populations of N_r MUs controlled by the experimental vector of MN spike trains, representative $f_{0,k}^{MU}$ values were derived from the $f_0^{MU}(k)$ distribution and assigned to the experimental MUs to account for the force-generating properties of the MUs not identified experimentally. In such case, the distribution of simulated MU forces (Figure 7B, C) was not physiological and interpretable. We showed that locating the N_r MUs into the real T^{th}-ranked MU pool with EQ. 6 before assigning representative $f_{0,k}^{MU}$ values (Figure 7C) corrected for the non-homogeneous distribution of the experimental samples across the MU pool, which was previously discussed, and allowed predictions accuracies of $F^M(t)$ close to those obtained with the complete population of N MUs (green dashed versus solid red traces in Figure 8, Table 4). For example, the few

947 low-threshold MUs identified with grids of low electrode density were assigned high representative
948 $f_{0,k}^{MU}$ values to represent the force-generating properties of the large population of small MUs that
949 were not identified experimentally. When the representative $f_{0,k}^{MU}$ values were assigned under the
950 assumption of a homogeneous distribution of the N_r MUs across the MU pool (Figure 7B), the
951 predictions of the whole muscle force were systematically less accurate, again under-evaluating the
952 force-generating activity of the low-threshold MU population.

953 Model scaling

954 The neuromuscular model developed in this study was scaled with the muscle-specific distribution of
955 MU maximum isometric forces $f_0^{MU}(k)$ derived from the literature (Figure 2) and the muscle
956 architectural parameters (Table 2) obtained from an MRI-based subjects-specific MSK model built with
957 automatic tools (Modenese & Kohout, 2020; Modenese & Renault, 2021). Therefore, the predictions
958 displayed in Figure 8 did not rely on any parameter calibration that would minimize external cost
959 functions, like commonly proposed in EMG-driven approaches (Pizzolato et al., 2015; Caillet et al.,
960 2022c). In particular, it is worth noting that the equations defining the model's force-generating
961 properties (EQ. 8 and EQ. 11 to EQ. 18) were tuned to match external experimental data independently
962 from the EMG and torque signals that were used in this study to control and validate the model. The
963 accurate prediction of the whole muscle force amplitude at 30% MVC in Figure 8E-G relied instead on
964 an estimation of muscle co-contraction during ankle dorsiflexion (Figure 5), a physiological and
965 comprehensive description of the neural drive, which the normalization of bEMG envelopes with
966 signals recorded at MVC cannot achieve, and an adequate distribution of the MU's maximum isometric
967 forces $f_{0,k}^{MU}$ across the modelled MU population, as discussed. In cases for which subject-specific
968 measurements are not possible or muscle-specific data are not as available in the literature as for the
969 TA, which is the case for most human muscles (Duchateau & Enoka, 2022), missing muscle architectural
970 parameters or the coefficients in EQ. 8 could be included in an optimization routine aiming to minimize
971 the difference between experimental and predicted joint torques, for example.

972

973 Interfacing the fields of motor control and MSK modelling

974 The neuromuscular model developed in this study brings together state-of-the-art experimental and
975 modelling techniques from the two complementary fields of motor control and MSK modelling. The
976 subject-specific neural control was obtained from recently developed experimental and processing
977 techniques (Figure 1A-C) that yielded the identification of much larger samples of discharging MUs
978 from recorded HDEMG signals than commonly obtained in the literature (Del Vecchio et al., 2020), i.e.,
979 up to 81 MUs in the TA muscle, and high ratios of low-threshold MUs (Caillet et al., 2023). The

980 neuromuscular model was scaled with subject-specific parameters derived from a subject-specific MSK
981 model (Figure 1H, I) compatible with the OpenSim platform (Delp et al., 2007; Seth et al., 2018), that
982 was built from the segmentation of MRI scans using state-of-the-art automated tools (Modenese &
983 Renault, 2021). The sampling of the neuromuscular model into individual Hill-type MUs opens avenues
984 to the control with experimental neural data of individual MU territories within volumetric muscle
985 actuators in MSK model. Volumetric muscle representations consistent with the segmented muscle
986 geometry and compatible with Opensim can be generated with recent automated tools (Modenese &
987 Kohout, 2020). Using recently developed ultrasound measurement techniques for tracking MU
988 twitches (Lubel et al., 2022; Lubel et al., 2023), the force-generating dynamics of the completely
989 reconstructed pool of N Hill-type MUs (Figure 7A, D) could be physiologically mapped to the lines of
990 actions constituting the volumetric muscle. This would provide a solution to the indeterminacy in EQ.
991 27 in Appendix A.2 by assigning MU-specific lengths $\overline{l_k}$ to the modelled MU actuators and would shift
992 the current approach towards a more physiological nonlinear summation of the MU forces based on
993 muscle architecture. This approach would also provide an adequate structure to model the force-
994 varying load path within the muscle tissue, as well as the mechanical interactions between MUs, the
995 resulting effect of which were experimentally observed (Lubel et al., 2022; Lubel et al., 2023). Finally,
996 this approach would enable the first MN-driven forward control of volumetric muscles at the level of
997 the individual MU actuator in neuromusculoskeletal simulations of human voluntary muscle
998 contraction, which allows the modelling of important phenomena like muscle and MU synergies (Del
999 Vecchio, Alessandro et al., 2023; Hug et al., 2023). This would further bridge the gap in modelling the
1000 interplay between motor control and resulting human motion.

1001

1002 Limitations

1003 Although the approach presented in Figure 1 provides a state-of-the-art approach for investigating and
1004 modelling the dynamics of the MU pool in forward simulations of human voluntary muscle contraction,
1005 it suffers from the following limitations. First, the muscle model was simplified to account for a rigid
1006 tendon. This approach was acceptable for the TA and decreased the computational load. Yet, the force
1007 equilibrium between the elastic tendon and the active muscle tissue should be considered with EQ. 28
1008 in Appendix A.2 for muscles with more compliant tendons or higher $\frac{l_s^T}{l_0^M}$ ratios, in which case $\bar{l}$ would
1009 vary and the PEE would not be neglected anymore. Second, the model is computationally more
1010 expensive than the classic single-input Hill-type actuators, which prevents its use in real-time
1011 investigations. As previously discussed (Caillet et al., 2022a), the computational load can be decreased
1012 by considering smaller reconstructed populations of 50 MUs without loss of accuracy in the estimated

1013 neural drive to muscle, or by, for example, simplifying the current model of MU excitation dynamics
1014 with an analytical description of the fibre APs instead of the 2nd-order ODE in EQ. 13. Third, the pipeline
1015 in Figure 1, although applicable to dynamic contractions, is currently constrained to isometric tasks
1016 due to experimental limitations in the decomposition of HDEMG signals into MU spike trains during
1017 motion. Although new computational approaches were recently developed for specific quasi-static
1018 (Oliveira & Negro, 2021) and dynamic (Glaser & Holobar, 2018) contraction protocols, small samples
1019 of 7-20 identified MUs were obtained, which is typically not sufficient to reliably control
1020 neuromuscular models, as discussed. Fourth, despite the decisive advantages vectors of identified MN
1021 spike trains provide compared to processed bEMGs, it remains challenging to obtain experimental
1022 samples of MUs that are representative of the true neural drive to muscle (Caillet et al., 2022a; Caillet
1023 et al., 2023). Fifth, physiologically describing the TA muscle with a MU resolution required assigning to
1024 the MU pool physiological distributions of neuromechanical parameters (Figure 2) obtained from TA-
1025 specific experimental measurements from the literature. Although multiple studies also investigated
1026 these parameters in the human thenar, ankle extensor, and masseter muscles, those properties
1027 remain mostly unknown for the other humans muscles, as recently reviewed (Duchateau & Enoka,
1028 2022). Sixth, the pipeline in Figure 1 was only applied to one subject in this study. Yet, the approach is
1029 general and can be reapplied to other subjects following the same method. Seventh, we had to correct
1030 a limitation of our reconstruction method (Caillet et al., 2022a) for the simulated MUs recruited during
1031 the plateau of constant recorded torque. When the discharge frequency of such simulated MU was
1032 below 7 Hz in average over the plateau, the predicted MU force was set to zero to avoid adding random
1033 noise to the predicted whole muscle force at the highest developed force levels.

1034

1035 Conclusion

1036 We developed the first MN-driven neuromuscular model of a population of individual Hill-type MUs
1037 controlled by a vector of dedicated experimental motoneuronal controls (Figure 1). The model
1038 distinguishes the dynamics of MU recruitment from rate coding and produces the whole muscle force
1039 as the summation of the forces generated by the individual modelled MUs. The model is subject-
1040 specific (Table 2), muscle-specific (Figure 2), and includes an advanced and physiological model of the
1041 MUs' activation dynamics (Figure 3, Figure 4, Table 1). The motoneuronal controls, derived from
1042 HDEMG signals, are experimental and decode the subject's intention, which makes the neuromuscular
1043 model applicable to the simulation and investigation of human voluntary muscle contraction. The
1044 model's predictions of the whole muscle force are sensitive to the quality of the experimental neural
1045 control. Accurate force predictions were obtained when the effective neural drive to muscle was

accurately estimated from the decoded MN spike trains (Figure 6C, Figure 8G), i.e., when the experimental samples of identified MUs were representative of the discharge activity of the complete MU pool. This was obtained when the muscle's myoelectric activity was recorded with large and dense grids of EMG electrodes during medium-force contractions, in which case the identified MUs span across the complete range of recruitment and are homogeneously distributed across the MU pool (Figure 6, Figure 8). Otherwise, the discharge activity of the low-threshold MUs is typically not identified, especially during high-force contractions, and the force predictions are inaccurate in the regions of low-force generation (Table 4). Inferring with a computational method the discharge activity of those MUs that were not identified experimentally improves the results to some extent and provides a window onto the continuous distribution of the MUs' force-generating dynamics across the MU pool. The accuracy of the force predictions also relies on a physiological assignment of the MU-specific force-generating properties to the modelled population of Hill-type MUs (Figure 8B-D). This MN-driven model advances the state-of-the-art of neuromuscular modelling, brings together the interfacing fields of motor control and MSK modelling, and finds applications in human-machine interfacing.

APPENDIX

A.1. Derivation of the experimental TA force

Methods

The force F_{cell} (in Volts) recorded by the load cell during the experiments was first converted into an ankle torque T (in N.m) using a constant gain derived from the load cell documentation and the geometry of the dynamometer. It was then assessed with EQ. 20, for the recordings made during the second session where bEMG electrodes were involved, the amount $\Delta T(t)$ of ankle torque taken over the trapezoidal contraction by agonist EHL, EDL and antagonist SOL, GM, and GL muscles. In EQ. 20, $T_i(t)$ is the ankle torque produced by the ith muscle, $\overline{EMG_i}(t)$ is the normalized EMG envelope for muscle i computed previously, L is the moment arm between the tendon of muscle i and the ankle joint previously measured from the subject-specific MSK model, $F_{0,i}^M$ is the maximum isometric force of muscle i estimated previously, and f_{FL} is the scaling factor calculated with the FL relationship in EQ. 11. $\overline{l_i^M}$ is the normalized length of muscle i and was calculated from the subject-muscle-specific l_i^{MT}, $l_{s,i}^T$, and $l_{0,i}^M$ values derived previously, assuming the tendons to be rigid. It was also assumed that the EDL and EHL muscles produced the same electrical activity.

$$\begin{gathered}\Delta T(t) = T_{EHL}(t) + T_{EDL}(t) - T_{GM}(t) - T_{GL}(t) - T_{SOL}(t) \\ T_i(t) = \overline{EMG_i}(t) \cdot L_i \cdot F_{0,i}^M \cdot f_{FL}\left(\overline{l_i^M}, \overline{EMG_i}\right) \\ \overline{l_i^M} = \frac{l_i^{MT} - l_{s,i}^T}{l_{0,i}^M}\end{gathered} \qquad \text{EQ. 20}$$

From EQ. 20, the continuous relationship between the level of load sharing $\Delta T(T)$ and the recorded ankle torque T was computed by fitting the exponential function in EQ. 21 to the $(T; \Delta T)$ cloud of points.

$$\Delta T(T) = a \cdot e^{b \cdot T} \qquad \text{EQ. 21}$$

The fitted $\Delta T(T)$ relationship in EQ. 21 was then applied to the torque $T(t)$ recorded during the first experimental session, for which the level of co-contraction $\Delta T\big(T(t)\big)$ was estimated. The experimental TA muscle force $F_{TA}(t)$ produced during the first experimental session was finally estimated with EQ. 22, where L_{TA} is the moment arm the TA tendon makes with the ankle joint.

$$F_{TA}(t)[N] = \frac{T(t) - \Delta T\big(T(t)\big)}{L_{TA}} \qquad \text{EQ. 22}$$

1085 Results

1086 During the second experimental session, voluntary ankle torques T (black dashed traces in Figure 9) of
1087 5.2, 8.8, and 17.5 Nm were recorded experimentally over the dorsiflexion tasks up to 30%, 50% and
1088 100% MVC, respectively. The results are of the same order of magnitude as the maximum voluntary
1089 torque of 22.5 Nm (+28%) calculated with published age-sex-dependent joint angle-torque
1090 relationships for ankle dorsiflexion (Anderson et al., 2007). Using the subject-muscle-specific
1091 properties of maximum isometric forces F_0^M and moment arms L reported in Table 2, a maximum
1092 torque in ankle dorsiflexion of 41 Nm was theoretically reachable for the participant if the TA, EDL, and
1093 EHL muscle produced their maximum force (maximum myoelectric activity at optimal length, i.e.,
1094 $\overline{EMG} = 1$ and $\bar{l} = 1$ in EQ. 20) and no co-contraction of the SOL, GM, and GL muscles occurred. In the
1095 conditions of the experiment, the TA, EDL, EHL, SOL, GM, and GL worked at 1.18, 0.78, 1.20, 0.60, 0.68,
1096 and 0.80 normalized lengths assuming rigid tendons, respectively (Table 2). The myoelectric activity of
1097 the EDL/EHL, SOL, GM, and GL muscles reached 27%, 5%, 3%, 6%, and 50%, 16%, 8%, 16%, and 100%,
1098 37%, 30%, 47% of their maximum recorded EMG amplitude, at 30% MVC, 50% MVC, and 100% MVC
1099 respectively.

1100 Very similar relationships $\Delta T(T)$, calculated with EQ. 20 and EQ. 21 with the subject-muscle-specific
1101 properties reported in Table 2, were obtained for both trapezoidal contractions up to 30% and 50%
1102 MVC between the amplitude of measured ankle torque $T(t)$ (black dashed traces in Figure 9) and the
1103 amount of ankle torque ΔT taken by the group of agnostic EHL and EDL and antagonist SOL, GM, and
1104 GL muscles (blue dotted traces in Figure 9). The average of the two relationships yielded the
1105 relationship in EQ. 23 (95% confidence ranges: [-0.1634 ; -0.1555] and [0.4380 ; 0.4441], $r^2 = 0.84$). EQ.
1106 23 suggests that contractile activities of the antagonist muscles SOL, GM, and GL overtook the ankle
1107 torque produced by the agonist EDL and EHL muscles following an exponential tendency with
1108 increasing recorded torques T with, for example, $\Delta T = -1.6\ Nm$ at $T = 5.2\ Nm$ (at 30% MVC) and
1109 $\Delta T = -7.7\ Nm$ at $T = 8.8\ Nm$ (at 50% MVC).

$$\Delta T(T)[N \cdot m] = -0.1595 \cdot e^{0.4411 \cdot T} \qquad \text{EQ. 23}$$

1110

1111 From EQ. 22, the force developed by the TA was estimated to reach 260 N and 656 N (torques displayed
1112 as solid red lines in Figure 9) at 30% and 50% MVC respectively, i.e. 25% and 63% of the TA's maximum
1113 isometric force F_0^M (Table 2), which seems reasonable for a participant who aimed to isolate the TA
1114 during those contractions. At 30% MVC and 50% MVC, the agonist EDL and EHL muscles collectively
1115 produced around 112 N and 215 N of force respectively, i.e., less than half the amount of force

produced by the TA muscle despite having more than half the force-generating capacities, which is again consistent with a participant who aimed to isolate the TA during those contractions.

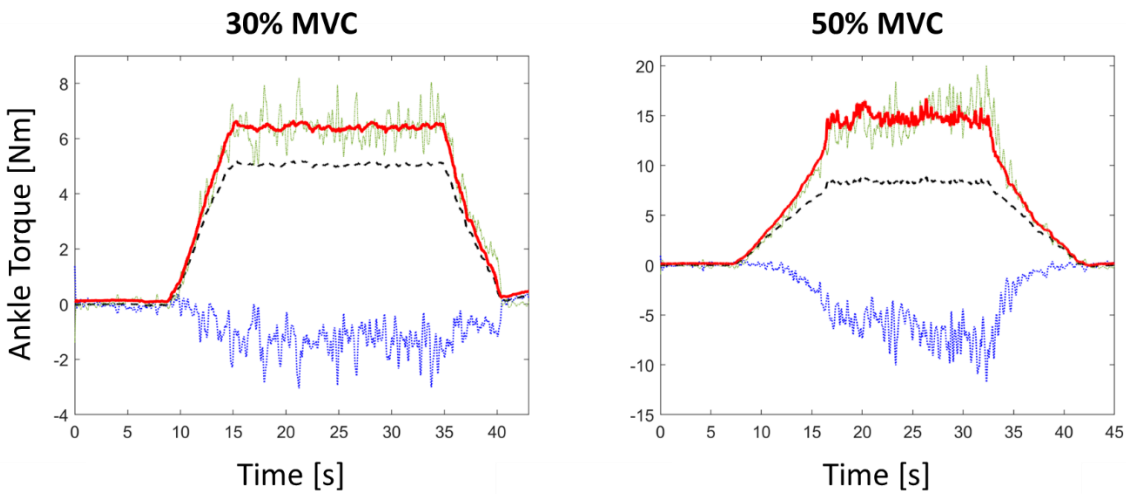

Figure 9: Estimation of the ankle torque developed by the TA muscle (solid red traces) from the recorded ankle torque T (dashed black traces) during the trapezoidal contractions up to 30% (Left) and 50% MVC (right) performed during the second experimental session. The amount of ankle torque ΔT produced by the agonist EDL and EHL and antagonist SOL, GM, and GL muscles (blue dotted traces) was calculated with EQ. 20 using the subject-muscle-specific properties reported in Table 2. ΔT was negative during the contractions, i.e., the agonist and antagonist muscle altogether produced a torque in plantarflexion. The ankle torque developed by the TA muscle was calculated as $T - \Delta T$ (green dash-dotted traces) and as $T - \Delta T(T)$ (solid red traces), where $\Delta T(T)$ given in EQ. 23 is the continuous relationship fitted to the $(T; \Delta T)$ cloud of points.

A.2. Physiological and mathematical steps taken to simplify the neuromuscular model

The MN-driven neuromuscular model developed in this study (Figure 1F) consists in a population of n in-parallel FGs, that describes the force-generating activity of the MU pool according to the cascading neuromuscular dynamics of the individual MUs in Figure 3. The FGs are placed in-parallel with a single muscle-scale passive elastic element (PEE) and in-series with a common in-series elastic element (SEE), i.e., the tendon. n is the length of the vector of available input spike trains controlling the model and takes the values N_r or N in this study.

The FGs individually develop the MU active forces $f_k^{MU}, k \in [\![1; n]\!]$, which linearly sum with the PEE force F^{PEE} to yield the total muscle force F^M. Neglecting the low pennation angle between the muscle belly and the tendon of the TA (approximately 11° (Rajagopal et al., 2016)), which may underestimate F^M by approximately 2%, F^M equals the tendon force F^{SEE} by equilibrium in EQ. 24.

$$F^M = \sum_{k=1}^{n} f_k^{MU} + F^{PEE} = F^{SEE} \qquad \text{EQ. 24}$$

This approach neglects both the geometrical orientation of the individual MUs and the lateral force transmission between MUs, both of which would decrease the total force developed by the MU pool along the tendon if considered.

In the following, all TA quantities are normalized with respect to the MU or whole muscle optimal length or maximum isometric force and are reported with a bar following EQ. 25. In EQ. 25, $f_{k,0}^{MU}$, $l_{k,0}^{MU}$, l_k^{MU}, and $\overline{v_k}$ are the maximum isometric force, the optimal length, the length, and the contraction velocity of the FG of MU k, respectively.

$$\overline{F^{PEE}} = \frac{F^{PEE}}{F_0^M} \qquad \overline{f_{k,0}^{MU}} = \frac{f_{k,0}^{MU}}{F_0^M}$$

$$\overline{F^{SEE}} = \frac{F^{SEE}}{F_0^M} \qquad \overline{f_k^{MU}} = \frac{f_k^{MU}}{F_0^M}$$

$$\overline{l^{MT}} = \frac{l^{MT}}{l_0^M} \qquad \overline{l_k} = \frac{l_k^{MU}}{l_{0,k}^{MU}} \qquad \text{EQ. 25}$$

$$\overline{v_k} = \frac{d\overline{l_k}}{dt}$$

The individual normalized MU forces $\overline{f_k^{MU}}$ produced by the MU FGs were modelled in EQ. 26 to be the linear product of the MU normalized maximum isometric force $\overline{f_{k,0}^{MU}}$, the MU active state a_k, the MU normalized force-length (FL) scaling factor f_{FL}, and the MU normalized force-velocity (FV) scaling factor f_{FV}.

$$\overline{f_k^{MU}}(a_k, \bar{l}_k, \bar{v}_k) = \overline{f_{k,0}^{MU}} \cdot a_k(\bar{l}_k) \cdot f_{FL}(a_k, \bar{l}_k) \cdot f_{FV}(a_k, \bar{l}_k, \bar{v}_k) \qquad \text{EQ. 26}$$

Inserting EQ. 26 into EQ. 24, it yields EQ. 27.

$$\overline{F^{SEE}} - \overline{F^{PEE}} = \sum_{k=1}^{n} \overline{f_{k,0}^{MU}} \cdot \left(a_k(\bar{l}_k) \cdot f_{FL}(a_k, \bar{l}_k) \cdot f_{FV}(a_k, \bar{l}_k, \bar{v}_k)\right) \qquad \text{EQ. 27}$$

EQ. 27 cannot be solved without knowing, for each MU, the value of its individual fibre architecture (optimal fibre length, fibre length), which implies knowing their spatial distribution, at all frames and active state. The muscle quantities are currently unfeasible to measure and therefore we implemented a number of simplifications displayed in Figure 10 and detailed in the following. First, it was assumed that all the MUs in the MU pool shared the same optimal MU length l_0^{MU}, which was taken to be the subject-specific muscle optimal length l_0^M derived previously in EQ. 2. Second, expecting the MU optimal lengths $l_{0,k}^{MU}$ to be related to the MU lengths l_k^{MU}, all the MUs in the MU pool were assigned a common (normalized) length $\bar{l} = \frac{l^{MU}}{l_0^M}$ and by extension a common normalized contraction velocity $\bar{v}$, as $\bar{v} = \frac{d\bar{l}}{dt}$. Third, to isolate $\bar{v} = \frac{d\bar{l}}{dt}$ and rearrange EQ. 27 as a differential equation of the common normalized MU length $\bar{l}$, the MU FV relationship f_{FV} was simplified to be independent from the individual MU active state a_k, which yielded EQ. 28.

$$\bar{v} = \frac{d\bar{l}}{dt} = f_{FV}^{-1}\left(\frac{\overline{F^{SEE}} - \overline{F^{PEE}}}{\sum_k \overline{f_{k,0}^{MU}} \cdot \left(a_k(\bar{l}) \cdot f_{FL}(a_k, \bar{l})\right)}\right) \qquad \text{EQ. 28}$$

Although EQ. 28 can be solved numerically for $\bar{l}$, the computational cost and the complexity of the model were further reduced by first assuming the TA tendon to be rigid {4}. As $\frac{l_s^T}{l_0^M} = 3.5$ for the participant's TA muscle, this assumption was judged acceptable for low-to-medium TA isometric contractions, considering that $\frac{l_s^T}{l_0^M} = 1$ describes a 'very stiff' tendon in the literature (Zajac Felix, 1989). With this assumption, the tendon length is constant and equals the tendon slack length (Millard et al., 2013) $l^{SEE} = l_s^T$. As l^{MT} is also constant during isometric contractions, so is the common normalized MU length $\bar{l}$, in which case $f_{FV} = 1$. Second, because $l^{MT} = l_s^T + 1.16 \cdot l_0^M$ for the segmented TA

muscle in the conditions of the experiment (see Results Section for the subject-specific values calculated with EQ. 2), it was finally approximated {5} that the FGs worked at the common normalized length $\bar{l} = 1.16$, in which case $\overline{F^{PEE}} = 0.02 \approx 0$, according to EQ. 29 with $k_1 = 5$ and $k_2 = 0.6$ for human young adults (Thelen, 2003).

$$\overline{F^{PEE}}(\bar{l}) = \begin{cases} 0 & ; \quad \bar{l} < 1 \\ \dfrac{e^{\frac{k_1}{k_2}(\bar{l}-1)} - 1}{e^{k_1} - 1} & ; \quad \bar{l} \geq 1 \end{cases} \qquad \text{EQ. 29}$$

With these five key simplifications {1-5}, the PEE and SEE (in grey in Figure 1F) were neglected and the rheological structure was reduced to the cohort of in-parallel MU actuators (in black in Figure 1F), the dynamics of which reduced to EQ. 10 in the main text of the manuscript

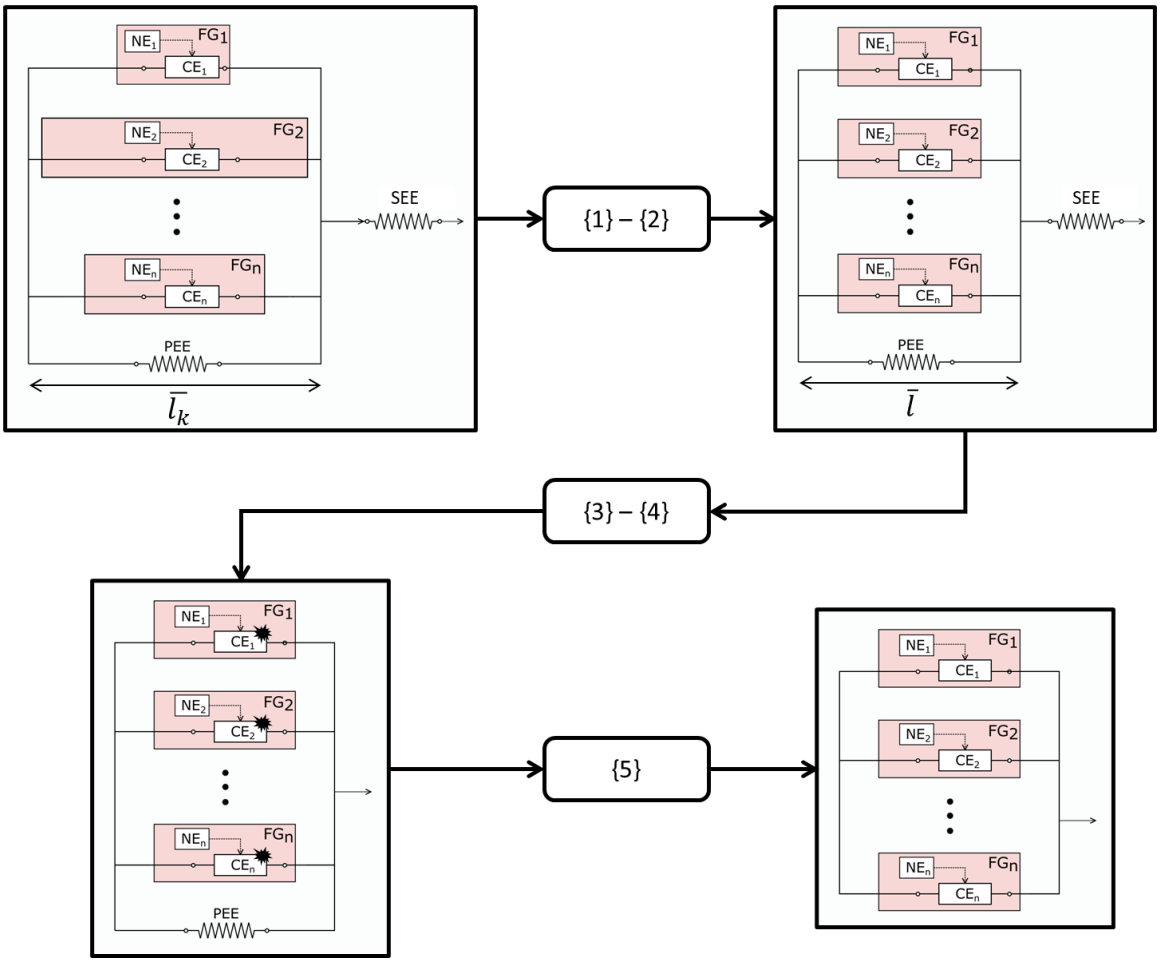

Figure 10: Step-by-step simplification of the MN-driven model. After neglecting the pennation angle between the TA muscle and tendon, the MUs are first assumed to share a common optimal length, which is the whole muscle's optimal length l_0^M {1} and a common normalized length $\bar{l}$ {2}. Then, the MUs' FV relationships are simplified to be activation-dependent {3}, before the tendon is assumed rigid {4}. Consequently, the SEE is neglected, the muscle contracts isometrically, and the FV relationship is neglected. Finally, based on subject-specific MSK measurements, it yields $\bar{l} = 1.16$, in which case the PEE develops negligible force and is neglected {5}.

A.3. Derivation of the free Calcium dynamics

Despite some disagreements (Haugen, 1991), it has been repeatedly observed in *in vitro* experiments on amphibian fibres from the semitendinosus, iliofibularis and TA muscles (Blinks et al., 1978; Baylor, S. M. et al., 1983; Close & Lännergren, 1984; Konishi et al., 1991) that the peak value of the calcium concentration nonlineary varies with the sarcomere length l^s. The experimental data provided by these studies was manually digitized and normalized to the highest peak $[Ca^{2+}]$ value retrieved in each study and to the optimal sarcomere length l_0^s $\left(\bar{l} = \frac{l^s}{l_0^s}\right)$, which is typically $2.1\mu m$ in these amphibian muscles. The piecewise linear trendline $f_1(\bar{l})$ given in EQ. 15 and displayed in Figure 11 was fitted to the normalized data, which reveals that the peak $[Ca^{2+}]$ value is obtained between 1.15 and 1.30 l_0^s.

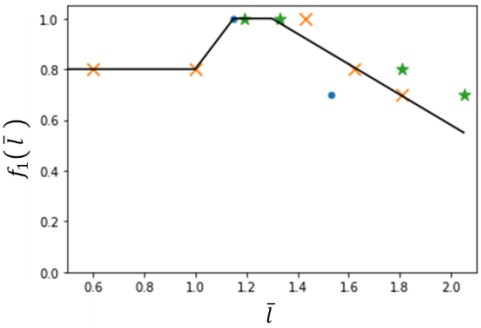

Figure 11: Nonlinear dependency of the peak Ca^{2+} concentration in muscle fibres from amphibian muscles to the normalized sarcomere length, directly scaled to fibre length. Blue dots (Blinks et al., 1978), green stars (Konishi et al., 1991), orange crosses (Close & Lännergren, 1984).

The $f_2(\bar{l})$ scaling factor described in EQ. 16 was obtained following a similar approach and models the linear increase in τ_d with longer normalized fibre lengths $\bar{l}$ above $1.15 l_0^s$ observed experimentally (Konishi et al., 1991).

In the literature of Hill-type muscle models, the coefficients scaling the mathematical equations describing the calcium transients (b_1, b_2, b_3 in EQ. 14) are typically tuned to match dated experimental observations of calcium waves obtained *in vitro* from amphibian muscle fibres in low-temperature baths (Caillet et al., 2022c). Yet, the calcium dynamics in the sarcoplasm are strongly species-dependent, which transients twice longer in amphibians than in mammals (Hollingworth, S. et al., 1996), and temperature-dependent (Blinks et al., 1978; Miledi et al., 1982; Eusebi et al., 1983; Hirota et al., 1989; Raju et al., 1989; Konishi et al., 1991; Delbono & Stefani, 1993; Delbono et al., 1995; Zhao et al., 1996; Capote et al., 2005; Hollingworth, Stephen et al., 2008; Baylor, Stephen M. & Hollingworth, 2011; Hollingworth, Stephen et al., 2012). Moreover, these dated experimental observations were typically obtained with chemical indicators (murexide, aequorin and arsenazo III for example) that have

a high affinity to components other than calcium ions in the myoplasm, such as Mg ions, and report calcium twitches of too low peak values and delayed transients. Because of these limitations, rather than considering the values proposed in Hatze's work (Hatze, 1977) for the b_1, b_2, b_3 coefficients, which were obtained in frog fibres at 9°C with the aequorin indicator, the b_1, b_2, b_3 coefficients were here tuned to match the experimental data from two experimental studies (Hollingworth, S. et al., 1996; Baylor, S. M. & Hollingworth, 2003), where the experimental $[Ca^{2+}]$ waves were measured at 28-35°C in rodent fibres with the reliable (Hirota et al., 1989; Konishi et al., 1991; Hollingworth, S. et al., 1996; Zhao et al., 1996; Baylor, S. M. & Hollingworth, 2003; Hollingworth, Stephen et al., 2008) mag-fura-2 indicator. Lacking human data in the literature, it was believed that the calcium dynamics in rodents at 35°C were the most representative for the human species at body temperature. Because both studies (Hollingworth, S. et al., 1996; Baylor, S. M. & Hollingworth, 2003) performed their experiments at the same sarcomere length $l^s = 3.8\mu m \approx 1.6 l_0^s$ (Rassier et al., 1999), the length-dependent scaling factors were set to $f_1(1.6) = 0.82$ and $f_2(1.6) = 0.82$ when tuning the b_1, b_2, b_3 coefficients.

A.4. Derivation of the Ca-Tn dynamics

As previously reported (Matsuo et al., 2010), cross-bridge formation increases the Ca^{2+} affinity of troponin and slows down Ca^{2+} detachment from troponin. When triggered by a single AP, the decay rate constant τ_d of the CaTn twitch therefore strongly decreases as the filamentary overlap decreases. In other terms, when $\bar{l}$ increases above 1.0, CaTn decays more rapidly. Consequently, the mag-2-fura measurements of CaTn, which overlook this affinity to cross-bridge formation, are not reliable at the sarcomere lengths for which filamentary overlap occurs, and the trajectory of the intensity of the meridional reflection from troponin at 1/38.5nm^{-1} must be used instead to measure CaTn (Matsuo et al., 2010).

In work from Matsuo et al. (Matsuo et al., 2010), experiments were performed in frogs at 16°C, in muscles of dominantly fast fibres at sarcomere lengths $l^s = 1.9 l_0^s$ (nonoverlap state) and $l^s = 1.3 l_0^s$ (overlap state). The experimental CaTn time traces were digitized and the t_{tp} and τ_d values were measured at both lengths l^s. To obtain CaTn values for rodents and slow fibres, the available experimental data (frog, fast fibre, 16°C) was extrapolated, in first approximation, to rodent data at 35°C in slow fibres by using the same species- temperature- and fibre type-scaling factors as used with the $[Ca^{2+}]$ transients previously investigated. In three steps, the t_{tp} and τ_d frog quantities were therefore gradually multiplied by 0.5, 0.44, and 2.5. Because the t_{tp} and τ_d values, initially measured at $l^s = 1.9 l_0^s$ and $l^s = 1.3 l_0^s$, linearly depend on the number of formed cross-bridges, piecewise linear length-dependent relationships $t_{tp}(\bar{l})$ and $\tau_d(\bar{l})$ were inferred (Table 5) from a typical piecewise-linear force-length shape (Rassier et al., 1999) corrected for rodent optimal sarcomere lengths $l_0^s = 2.4\mu m$. Finally, the CaTn peak-to-peak amplitude was set to $120\mu M$ and $220\mu M$ for slow and fast fibres respectively (Baylor, S. M. & Hollingworth, 2003; Baylor, Stephen M. & Hollingworth, 2007; Baylor, Stephen M. & Hollingworth, 2012).

As before, the $f_3(\bar{l}), f_4(\bar{l}), f_5(\bar{l})$ length-dependent scaling factors and the c_1, c_2, P_0 parameters, respectively reported in Table 5 and Table 1, were tuned so that the output of the differential equation in EQ. 17 matched the scaled experimental length-dependent t_{tp} and τ_d, and A_t quantities in the first column of Table 5 with less than 5% error.

Table 5: (Left) Typical t_{tp}, τ_d and A_t values of the CaTn concentration twitch in rodent fast and slow fibres, and their length-dependencies, inferred from experimental amphibian data. (Right) Description of the length-dependent scaling factors in EQ. 17.

$[Ca-Tn]$ metrics	Length-dependent scaling factors
$t_{tp,fast}(\bar{l}) = \begin{cases} 6ms \;\; if\ \bar{l} < 0.7 \\ 2 + 5\bar{l} \;\; if\ \bar{l} \in [0.7; 0.97] \\ 7ms\ if\ \bar{l} \in [0.97; 1.02] \\ 12 - 5\bar{l} \;\; if\ \bar{l} \in [1.02; 1.6] \\ 4ms \;\; if\ \bar{l} > 1.6 \end{cases}$	$\begin{cases} f_3(\bar{l}) = 0.33 & if\ \bar{l} \leq 0.7 \\ f_3(\bar{l}) = 0.33 + 2.47(\bar{l} - 0.75) & if\ \bar{l} \leq 0.97 \\ f_3(\bar{l}) = 1.0 & if\ 0.97 \leq \bar{l} \leq 1.02 \\ f_3(\bar{l}) = 8.9 - 11.73\bar{l} + 3.90\,\bar{l}^2 & if\ 1.02 \leq \bar{l} \leq 1.6 \\ f_3(\bar{l}) = 0.125 & if\ \bar{l} > 1.6 \end{cases}$
$\tau_{d,fast}(\bar{l}) = \begin{cases} 15ms \;\; if\ \bar{l} < 0.7 \\ -1 + 23\bar{l} \;\; if\ \bar{l} \in [0.7; 0.97] \\ 21ms\ if\ \bar{l} \in [0.97; 1.02] \\ 44 - 23\bar{l} \;\; if\ \bar{l} \in [1.02; 1.6] \\ 8ms \;\; if\ \bar{l} > 1.6 \end{cases}$	$\begin{cases} f_5(\bar{l}) = 0.75 & if\ \bar{l} \leq 0.7 \\ f_5(\bar{l}) = 0.75 + 0.94(\bar{l} - 0.75) & if\ \bar{l} \leq 0.97 \\ f_5(\bar{l}) = 1.0 & if\ 0.97 \leq \bar{l} \leq 1.02 \\ f_5(\bar{l}) = 0.9 + 0.84\bar{l} - 0.75\,\bar{l}^2 & if\ 1.02 \leq \bar{l} \leq 1.6 \\ f_5(\bar{l}) = 0.34 & if\ \bar{l} > 1.6 \end{cases}$
$A_{t,fast} = 220\mu M$	$\begin{cases} f_4(\bar{l}) = 1.09 & if\ \bar{l} \leq 0.7 \\ f_4(\bar{l}) = 1.09 - 0.32(\bar{l} - 0.75) & if\ \bar{l} \leq 0.97 \\ f_4(\bar{l}) = 1.0 & if\ 0.97 \leq \bar{l} \leq 1.02 \\ f_4(\bar{l}) = -4.4 + 8.24\bar{l} - 2.84\,\bar{l}^2 & if\ 1.02 \leq \bar{l} \leq 1.6 \\ f_4(\bar{l}) = 1.46 & if\ \bar{l} > 1.6 \end{cases}$
$t_{tp,slow}(\bar{l}) = \begin{cases} 11ms \;\; if\ \bar{l} < 0.7 \\ 4 + 10\bar{l} \;\; if\ \bar{l} \in [0.7; 0.97] \\ 14ms\ if\ \bar{l} \in [0.97; 1.02] \\ 24 - 10\bar{l} \;\; if\ \bar{l} \in [1.02; 1.6] \\ 8ms \;\; if\ \bar{l} > 1.6 \end{cases}$	$\begin{cases} f_3(\bar{l}) = 0.75 & if\ \bar{l} \leq 0.7 \\ f_3(\bar{l}) = 0.75 + 0.93(\bar{l} - 0.75) & if\ \bar{l} \leq 0.97 \\ f_3(\bar{l}) = 1.0 & if\ 0.97 \leq \bar{l} \leq 1.02 \\ f_3(\bar{l}) = 1.2 - 0.01\bar{l} - 0.22\,\bar{l}^2 & if\ 1.02 \leq \bar{l} \leq 1.6 \\ f_3(\bar{l}) = 0.67 & if\ \bar{l} > 1.6 \end{cases}$
$\tau_{d,slow}(\bar{l}) = \begin{cases} 38ms \;\; if\ \bar{l} < 0.7 \\ -3 + 57\bar{l} \;\; if\ \bar{l} \in [0.7; 0.97] \\ 52ms\ if\ \bar{l} \in [0.97; 1.02] \\ 110 - 57\bar{l} \;\; if\ \bar{l} \in [1.02; 1.6] \\ 19ms \;\; if\ \bar{l} > 1.6 \end{cases}$	$\begin{cases} f_5(\bar{l}) = 0.66 & if\ \bar{l} \leq 0.7 \\ f_5(\bar{l}) = 0.66 + 1.27(\bar{l} - 0.75) & if\ \bar{l} \leq 0.97 \\ f_5(\bar{l}) = 1.0 & if\ 0.97 \leq \bar{l} \leq 1.02 \\ f_5(\bar{l}) = 4.2 - 4.28\bar{l} - 1.11\,\bar{l}^2 & if\ 1.02 \leq \bar{l} \leq 1.6 \\ f_5(\bar{l}) = 0.21 & if\ \bar{l} > 1.6 \end{cases}$
$A_{t,slow} = 120\mu M$	$\begin{cases} f_4(\bar{l}) = 1.06 & if\ \bar{l} \leq 0.7 \\ f_4(\bar{l}) = 1.06 - 0.23(\bar{l} - 0.75) & if\ \bar{l} \leq 0.97 \\ f_4(\bar{l}) = 1.0 & if\ 0.97 \leq \bar{l} \leq 1.02 \\ f_4(\bar{l}) = 4.5 - 5.09\bar{l} + 1.62\,\bar{l}^2 & if\ 1.02 \leq \bar{l} \leq 1.6 \\ f_4(\bar{l}) = 0.52 & if\ \bar{l} > 1.6 \end{cases}$

A.5. Derivation of the dynamics of MU activation

The d_i coefficients in EQ. 18 were tuned so that the predicted MU active state produced by a CaTn twitch matched the normalized experimental twitch torque or force $\overline{f^{tw}}$ recorded in individual human MUs in the TA muscle (Andreassen & Arendt-Nielsen, 1987; Van Cutsem et al., 1997; Van Cutsem et al., 1998). Although the experimental $\overline{f^{tw}}$ also accounts for mechanical dynamics other than the activation dynamics, such as the muscle-tendon interplay or muscle co-contraction and may not be a precise indicator of the MU active state, it remains the only available metric for a in the human literature. Because the physiological length-dependency of the cross-bridge attachment dynamics at known Ca-Tn concentration P is unclear in the literature, the d_1, d_2 and d_3 parameters were modelled constant at all lengths and were calibrated at optimal length $\bar{l} = 1.0$. Although it is debated in the literature, as previously reviewed (Caillet et al., 2022b), whether the MU type is correlated to t_{tp} and $t_{0.5}$, it was assumed for simplicity that the slow-type MUs had the longest time-to-peak and half relaxation time values in the MU pool. Considering that 12% of the MUs are of the fast type in the MU pool (Figure 2D), and assuming that 12% of the MUs identified in the aforementioned experimental TA literature were of the fast type, it was derived from the t_{tp} and $t_{0.5}$ bar plot distributions in these studies that the slow and fast type MUs respectively had t_{tp} values in the $[35-90]ms$ and $[20-35]ms$ ranges, of weighted average 50ms and 30ms, and $t_{0.5}$ values in the $[50-90]ms$ and $[40-50]ms$ ranges, of weighted average 65 and 42ms. Finally, d_1 was tuned so that the active state reached 1.0 at 50 Hz stimulation, as firing frequencies above 50Hz were never reported in the human literature.

REFERENCES

Anderson DE, Madigan ML, Nussbaum MA (2007) Maximum voluntary joint torque as a function of joint angle and angular velocity: Model development and application to the lower limb. J.Biomech. 40:3105-3113.

Andreassen S, Arendt-Nielsen L (1987) Muscle fibre conduction velocity in motor units of the human anterior tibial muscle: A new size principle parameter. J. Physiol. 391:561-571.

Ao D, Song R, Gao J (2017) Movement performance of human-robot cooperation control based on EMG-driven hill-type and proportional models for an ankle power-assist exoskeleton robot. TNSRE 25:1125-1134.

Arabadzhiev TI, Dimitrov GV, Dimitrova NA (2005) Intracellular action potential generation and extinction strongly affect the sensitivity of M-wave characteristic frequencies to changes in the peripheral parameters with muscle fatigue. Journal of Electromyography and kinesiology 15:159-169.

Balog EM, Thompson LV, Fitts RH (1994) Role of sarcolemma action potentials and excitability in muscle fatigue. J.Appl.Physiol. 76:2157-2162.

Baylor SM, Hollingworth S (2003) Sarcoplasmic reticulum calcium release compared in slow-twitch and fast-twitch fibres of mouse muscle. J.Physiol.(Lond.) 551:125-138.

Baylor SM, Chandler WK, Marshall MW (1983) Sarcoplasmic reticulum calcium release in frog skeletal muscle fibres estimated from arsenazo III calcium transients. J.Physiol.(Lond.) 344:625-666.

Baylor SM, Hollingworth S (2012) Intracellular calcium movements during excitation–contraction coupling in mammalian slow-twitch and fast-twitch muscle fibers. J.Gen.Physiol. 139:261-272.

Baylor SM, Hollingworth S (2011) Calcium indicators and calcium signalling in skeletal muscle fibres during excitation–contraction coupling. Prog.Biophys.Mol.Biol. 105:162-179.

Baylor SM, Hollingworth S (2007) Simulation of Ca2 movements within the sarcomere of fast-twitch mouse fibers stimulated by action potentials. J.Gen.Physiol. 130:283-302.

Bigland-Ritchie B, Fuglevand AJ, Thomas CK (1998) Contractile properties of human motor units: Is man a cat? The Neuroscientist 4:240-249.

Binder-Markey BI, Persad LS, Shin AY, Litchy WJ, Kaufman KR, Lieber RL (2023) Direct intraoperative measurement of isometric contractile properties in living human muscle. J.Physiol.(Lond.) .

Blinks JR, Rüdel R, Taylor SR (1978) Calcium transients in isolated amphibian skeletal muscle fibres: Detection with aequorin. J.Physiol.(Lond.) 277:291-323.

Brooks JE, Hongdalarom T (1968) Intracellular electromyography: Resting and action potentials in normal human muscle. Arch.Neurol. 18:291-300.

Burkholder TJ, Lieber RL (2001) Sarcomere length operating range of vertebrate muscles during movement. J.Exp.Biol. 204:1529-1536.

Caggiano V, Wang H, Durandau G, Sartori M, Kumar V (2022) MyoSuite--A contact-rich simulation suite for musculoskeletal motor control. arXiv preprint arXiv:2205.13600 .

Caillet AH, Phillips AT, Farina D, Modenese L (2022a) Estimation of the firing behaviour of a complete motoneuron pool by combining electromyography signal decomposition and realistic motoneuron modelling. PLOS Computational Biology 18:e1010556, doi: https://doi.org/10.1371/journal.pcbi.1010556

Caillet AH, Phillips AT, Farina D, Modenese L (2022b) Mathematical relationships between spinal motoneuron properties. eLife 11:e76489, doi: https://doi.org/10.7554/eLife.76489

Caillet AH, Avrillon S, Kundu A, Yu T, Phillips AT, Modenese L, Farina D (2023) Larger and denser: An optimal design for surface grids of EMG electrodes to identify greater and more representative samples of motor units. bioRxiv 2023.02. 18.529050, doi: https://doi.org/10.1101/2023.02.18.529050

Caillet AH, Phillips AT, Carty C, Farina D, Modenese L (2022c) Hill-type computational models of muscle-tendon actuators: A systematic review. bioRxiv, doi: https://doi.org/10.1101/2022.10.14.512218.

Callahan DM, Umberger BR, Kent-Braun JA (2013) A computational model of torque generation: Neural, contractile, metabolic and musculoskeletal components. PloS one 8:e56013.

Capote J, Bolaños P, Schuhmeier RP, Melzer W, Caputo C (2005) Calcium transients in developing mouse skeletal muscle fibres. J.Physiol.(Lond.) 564:451-464.

Carriou V, Boudaoud S, Laforet J, Mendes A, Canon F, Guiraud D (2019) Multiscale hill-type modeling of the mechanical muscle behavior driven by the neural drive in isometric conditions. Computers in biology and medicine 115:103480.

Celichowski J, Grottel K (1993) Twitch/tetanus ratio and its relation to other properties of motor units. Neuroreport 5:201-204.

Cignoni, P.,Callieri, M.,Corsini, M.,Dellepiane, M.,Ganovelli, F.,Ranzuglia, G.(2008) Meshlab: An open-source mesh processing tool. **2008**, 129-136.

Cimolato A, Driessen JJ, Mattos LS, De Momi E, Laffranchi M, De Michieli L (2022) EMG-driven control in lower limb prostheses: A topic-based systematic review. Journal of NeuroEngineering and Rehabilitation 19:1-26.

Close RI, Lännergren JI (1984) Arsenazo III calcium transients and latency relaxation in frog skeletal muscle fibres at different sarcomere lengths. J.Physiol.(Lond.) 355:323-344.

Cutsem MV, Feiereisen P, Duchateau J, Hainaut K (1997) Mechanical properties and behaviour of motor units in the tibialis anterior during voluntary contractions. Canadian journal of applied physiology 22:585-597.

De Luca CJ, Hostage EC (2010) Relationship between firing rate and recruitment threshold of motoneurons in voluntary isometric contractions. J.Neurophysiol. 104:1034-1046.

De Luca CJ (1997) The use of surface electromyography in biomechanics. Journal of applied biomechanics 13:135-163.

Del Vecchio A, Holobar A, Falla D, Felici F, Enoka RM, Farina D (2020) Tutorial: Analysis of motor unit discharge characteristics from high-density surface EMG signals. Journal of Electromyography and Kinesiology 53:102426.

Del Vecchio A, Germer CM, Kinfe TM, Nuccio S, Hug F, Eskofier B, Farina D, Enoka RM (2023) The forces generated by agonist muscles during isometric contractions arise from motor unit synergies. Journal of Neuroscience .

Delbono O, O'rourke KS, Ettinger WH (1995) Excitation-calcium release uncoupling in aged single human skeletal muscle fibers. J.Membr.Biol. 148:211-222.

Delbono O, Stefani E (1993) Calcium transients in single mammalian skeletal muscle fibres. J.Physiol.(Lond.) 463:689-707.

Delp SL, Anderson FC, Arnold AS, Loan P, Habib A, John CT, Guendelman E, Thelen DG (2007) OpenSim: Open-source software to create and analyze dynamic simulations of movement. TBME 54:1940-1950.

Dick TJM, Biewener AA, Wakeling JM (2017) Comparison of human gastrocnemius forces predicted by hill-type muscle models and estimated from ultrasound images. Journal of experimental biology 220:1643-1653.

Dick TJ, Hug F (2023) Advances in imaging for assessing the design and mechanics of skeletal muscle in vivo. J.Biomech. 111640.

Dillmann U, Hopf HC, Lüder G, Schimrigk K (1996) Isometric muscle contractions after double pulse stimulation. comparison of healthy subjects and patients with myotonic dystrophy. Eur.J.Appl.Physiol.Occup.Physiol. 74:219-226.

Ding J, Wexler AS, Binder-Macleod SA (2000) Development of a mathematical model that predicts optimal muscle activation patterns by using brief trains. Journal of Applied Physiology 88:917-925.

Dorgan SJ, O'Malley MJ (1997) A nonlinear mathematical model of electrically stimulated skeletal muscle. T-RE 5:179-194.

Duchateau J, Enoka RM (2022) Distribution of motor unit properties across human muscles. J.Appl.Physiol. 132:1-13.

Dumitru D, King JC (1999) Motor unit action potential duration and muscle length. Muscle Nerve 22:1188-1195.

Ebashi S, Endo M (1968) Calcium and muscle contraction. Prog.Biophys.Mol.Biol. 18:123-183.

Elek JM, Kossev A, Dengler R, Schubert M, Wohlfahrt K, Wolf W (1992) Parameters of human motor unit twitches obtained by intramuscular microstimulation. Neuromuscul. Disord. 2:261-267.

Eusebi F, Miledi R, Takahashi T (1983) Aequorin-calcium transients in frog twitch muscle fibres. J.Physiol.(Lond.) 340:91-106.

Farina D, Vujaklija I, Brånemark R, Bull AMJ, Dietl H, Graimann B, Hargrove LJ, Hoffmann K, Huang H, Ingvarsson T, Janusson HB, Kristjánsson K, Kuiken T, Micera S, Stieglitz T, Sturma A, Tyler D, Weir RFf, Aszmann OC (2021) Toward higher-performance bionic limbs for wider clinical use. Nature biomedical engineering 1-13.

Farina D, Vujaklija I, Sartori M, Kapelner T, Negro F, Jiang N, Bergmeister K, Andalib A, Principe J, Aszmann OC (2017) Man/machine interface based on the discharge timings of spinal motor neurons after targeted muscle reinnervation. Nature biomedical engineering 1:1-12.

Farina D, Negro F (2015) Common synaptic input to motor neurons, motor unit synchronization, and force control. Exercise and sport sciences reviews 43:23-33.

Farmer TW, Buchthal F, Rosenfalck P (1960) Refractory period of human muscle after the passage of a propagated action potential. Electroencephalogr.Clin.Neurophysiol. 12:455-466.

Ferguson, R. A. & Shur, N. F. (2022) Skeletal muscle biopsy: Techniques and applications. In Anonymous *Sport and Exercise Physiology Testing Guidelines.* Routledge, pp. 205-211.

Fuglevand AJ, Winter DA, Patla AE (1993) Models of recruitment and rate coding organization in motor-unit pools. Journal of neurophysiology 70:2470-2488.

Fuglevand AJ, Macefield VG, Bigland-Ritchie B (1999) Force-frequency and fatigue properties of motor units in muscles that control digits of the human hand. J Neurophysiol 81:1718-1729.

Glaser V, Holobar A (2018) Motor unit identification from high-density surface electromyograms in repeated dynamic muscle contractions. IEEE Transactions on Neural Systems and Rehabilitation Engineering 27:66-75.

Gogeascoechea, A.,Kobayashi, R.O.,Yavuz, U.S.,Sartori, M.(2021) Identification of motor unit twitch properties in the intact human in vivo. , 6310-6313.

Gollapudi SK, Lin DC (2009) Experimental determination of sarcomere force–length relationship in type-I human skeletal muscle fibers. J.Biomech. 42:2011-2016.

Gordon, Huxley, Julian (1966) The variation in isometric tension with sarcomere length in vertebrate muscle fibres. The Journal of physiology 184:170-192.

Hamouda A, Kenney L, Howard D (2016) Dealing with time-varying recruitment and length in hill-type muscle models. Journal of biomechanics 49:3375-3380.

Handsfield GG, Meyer CH, Hart JM, Abel MF, Blemker SS (2014) Relationships of 35 lower limb muscles to height and body mass quantified using MRI. J.Biomech. 47:631-638.

Hatze H (1980) *Myocybernetic Control Models of Skeletal Muscle - Characteristics and Applications.* University of South Africa Press, Pretoria, .

Hatze H (1977) A myocybernetic control model of skeletal muscle. Biological cybernetics 25:103-119.

Haugen P (1991) Calcium transients in skeletal muscle fibres under isometric conditions and during and after a quick stretch. Journal of Muscle Research & Cell Motility 12:566-578.

Heckman CJ, Enoka RM (2012) Motor unit. Compr. Physiol. 2:2629-2682.

Henneman E (1981) Recruitment of motoneurons : The size principle. Motor Unit Types, Recruitment and Plasticity in Health and Disease 26-60.

Henriksson-Larsén KB, Lexell J, Sjöström M (1983) Distribution of different fibre types in human skeletal muscles. I. method for the preparation and analysis of cross-sections of whole tibialis anterior. Histochem.J. 15:167-178.

Highlander, M. M.,Allen, J.M.,Elbasiouny, S.M.(2020) Meta-analysis of biological variables' impact on spinal motoneuron electrophysiology data. Journal of Neurophysiology, **123**, 1380.

Hirota A, Chandler WK, Southwick PL, Waggoner AS (1989) Calcium signals recorded from two new purpurate indicators inside frog cut twitch fibers. J.Gen.Physiol. 94:597-631.

Hof AL, Van den Berg J (1981) EMG to force processing I: An electrical analogue of the hill muscle model. Journal of biomechanics 14:747,755-753,758.

Hollingworth S, Zhao M, Baylor SM (1996) The amplitude and time course of the myoplasmic free [Ca2] transient in fast-twitch fibers of mouse muscle. J.Gen.Physiol. 108:455-469.

Hollingworth S, Kim MM, Baylor SM (2012) Measurement and simulation of myoplasmic calcium transients in mouse slow-twitch muscle fibres. J.Physiol.(Lond.) 590:575-594.

Hollingworth S, Zeiger U, Baylor SM (2008) Comparison of the myoplasmic calcium transient elicited by an action potential in intact fibres of mdx and normal mice. J.Physiol.(Lond.) 586:5063-5075.

Hug F, Avrillon S, Ibáñez J, Farina D (2023) Common synaptic input, synergies and size principle: Control of spinal motor neurons for movement generation. J.Physiol.(Lond.) 601:11-20.

Hussein M, Shebl S, Elnemr R, Elkaranshawy H (2022) A new muscle activation dynamics model, that simulates the calcium kinetics and incorporates the role of store-operated calcium entry channels, to enhance the electromyography-driven hill-type models. J.Biomech.Eng. 144:.

Hussein M, Shebl S, Elnemr R, Elkaranshawy H (2021) A new muscle activation dynamics model, that simulates the calcium kinetics and incorporates the role of store-operated calcium entry channels, to enhance the electromyography-driven hill-type models. J.Biomech.Eng. 144:011002.

Huxley, Niedergerke (1954) Structural changes in muscle during contraction: Interference microscopy of living muscle fibres. Nature 173:971-973.

Kapelner T, Sartori M, Negro F, Farina D (2020) Neuro-musculoskeletal mapping for man-machine interfacing. Scientific reports 10:1-10.

Kaufman KR, An K, Litchy WJ, Chao E (1991) Physiological prediction of muscle forces—I. theoretical formulation. Neuroscience 40:781-792.

Kim G, Ferdjallah MM, McKenzie FD (2013) An empirical muscle intracellular action potential model with multiple erlang probability density functions based on a modified newton method. Biomedical Engineering and Computational Biology 5:BECB. S11646.

Konishi M, Hollingworth S, Harkins AB, Baylor SM (1991) Myoplasmic calcium transients in intact frog skeletal muscle fibers monitored with the fluorescent indicator furaptra. J.Gen.Physiol. 97:271-301.

Kopec J, Delbeke J, McComas AJ (1978) Refractory period studies in a human neuromuscular preparation. Journal of Neurology, Neurosurgery & Psychiatry 41:54-64.

Legreneur P, Morlon B, Van Hoecke J (1996) Simulation of in situ soleus isometric force output as a function of neural excitation. Journal of biomechanics 29:1455-1462.

Lloyd DG, Besier TF (2003) An EMG-driven musculoskeletal model to estimate muscle forces and knee joint moments in vivo. Journal of Biomechanics 36:765-776.

Lubel E, Grandi Sgambato B, Rohlen R, Ibanez J, Barsakcioglu D, Tang M, Farina D (2023) Non-linearity in motor unit velocity twitch dynamics: Implications for ultrafast ultrasound source separation. bioRxiv 2023.03. 24.533983.

Lubel E, Sgambato BG, Barsakcioglu DY, Ibáñez J, Tang M, Farina D (2022) Kinematics of individual muscle units in natural contractions measured in vivo using ultrafast ultrasound. Journal of Neural Engineering 19:056005.

Ludin HP (1969) Microelectrode study of normal human skeletal muscle. Eur.Neurol. 2:340-347.

Macefield VG, Fuglevand AJ, Bigland-Ritchie B (1996) Contractile properties of single motor units in human toe extensors assessed by intraneural motor axon stimulation. J Neurophysiol 75:2509-2519.

Manuel M, Chardon M, Tysseling V, Heckman CJ (2019) Scaling of motor output, from mouse to humans. Physiology (Bethesda, Md.) 34:5-13.

Matsuo T, Iwamoto H, Yagi N (2010) Monitoring the structural behavior of troponin and myoplasmic free Ca2 concentration during twitch of frog skeletal muscle. Biophys.J. 99:193-200.

Miledi R, Parker I, Zhu PH (1982) Calcium transients evoked by action potentials in frog twitch muscle fibres. J.Physiol.(Lond.) 333:655-679.

Millard M, Uchida T, Seth A, Delp SL (2013) Flexing computational muscle: Modeling and simulation of musculotendon dynamics. Journal of biomechanical engineering 135:021005.

Milner-Brown HS, Stein RB, Yemm R (1973) The orderly recruitment of human motor units during voluntary isometric contractions. J. Physiol. 230:359-370.

Modenese L, Renault J (2021) Automatic generation of personalised skeletal models of the lower limb from three-dimensional bone geometries. J.Biomech. 116:110186.

Modenese L, Kohout J (2020) Automated generation of three-dimensional complex muscle geometries for use in personalised musculoskeletal models. Ann.Biomed.Eng. 48:1793-1804.

Möller TB & Reif, E (2007) *Pocket Atlas of Sectional Anatomy.* thieme, .

Moo EK, Leonard TR, Herzog W (2020) The sarcomere force–length relationship in an intact muscle–tendon unit. J.Exp.Biol. 223:jeb215020.

Muceli S, Poppendieck W, Holobar A, Gandevia S, Liebetanz D, Farina D (2022) Accurate decoding of the spinal cord output in humans with implanted high-density electrode arrays. bioRxiv .

Negro F, Muceli S, Castronovo AM, Holobar A, Farina D (2016) Multi-channel intramuscular and surface EMG decomposition by convolutive blind source separation. JNE 13:026027.

Negro F, Yavuz U, Farina D (2016) The human motor neuron pools receive a dominant slow-varying common synaptic input. J. Physiol. 594:5491-5505.

Oliveira AS, Negro F (2021) Neural control of matched motor units during muscle shortening and lengthening at increasing velocities. J.Appl.Physiol. 130:1798-1813.

Pincheira PA, Boswell MA, Franchi MV, Delp SL, Lichtwark GA (2022) Biceps femoris long head sarcomere and fascicle length adaptations after 3 weeks of eccentric exercise training. Journal of Sport and Health Science 11:43-49.

Pizzolato C, Lloyd DG, Sartori M, Ceseracciu E, Besier TF, Fregly BJ, Reggiani M (2015) CEINMS: A toolbox to investigate the influence of different neural control solutions on the prediction of muscle excitation and joint moments during dynamic motor tasks. J.Biomech. 48:3929-3936.

Raikova R, Celichowski J, Angelova S, Krutki P (2018) A model of the rat medial gastrocnemius muscle based on inputs to motoneurons and on an algorithm for prediction of the motor unit force. Journal of neurophysiology 120:1973-1987.

Rajagopal A, Dembia CL, DeMers MS, Delp DD, Hicks JL, Delp SL (2016) Full-body musculoskeletal model for muscle-driven simulation of human gait. TBME 63:2068-2079.

Raju B, Murphy E, Levy LA, Hall RD, London RE (1989) A fluorescent indicator for measuring cytosolic free magnesium. American Journal of Physiology-Cell Physiology 256:C540-C548.

Rassier DE, MacIntosh BR, Herzog W (1999) Length dependence of active force production in skeletal muscle. J.Appl.Physiol. 86:1445-1457.

Sartori M, Yavuz U, Farina D (2017) In vivo neuromechanics: Decoding causal motor neuron behavior with resulting musculoskeletal function. Scientific reports 7:13465-14.

Sartori M, Reggiani M, Farina D, Lloyd DG (2012) EMG-driven forward-dynamic estimation of muscle force and joint moment about multiple degrees of freedom in the human lower extremity. PloS one 7:e52618.

Schmitt S, Günther M, Häufle DFB (2019) The dynamics of the skeletal muscle: A systems biophysics perspective on muscle modeling with the focus on hill-type muscle models. Mitteilungen der Gesellschaft für Angewandte Mathematik und Mechanik 42:n/a.

Seth A, Hicks JL, Uchida TK, Habib A, Dembia CL, Dunne JJ, Ong CF, Demers MS, Rajagopal A, Millard M, Hamner SR, Arnold EM (2018) OpenSim: Simulating musculoskeletal dynamics and neuromuscular control to study human and animal movement. PLoS computational biology 14:e1006223.

Song D, Raphael G, Lan N, Loeb GE (2008) Computationally efficient models of neuromuscular recruitment and mechanics. Journal of neural engineering 5:175-184.

Sun L, Sun Y, Huang Z, Hou J, Wu J (2018) Improved hill-type musculotendon models with activation-force-length coupling. Technology and Health Care 26:909-920.

Thelen DG (2003) Adjustment of muscle mechanics model parameters to simulate dynamic contractions in older adults. J Biomech Eng 125:70-77.

Thomas CK, Bigland-Richie B, Johansson RS (1991) Force-frequency relationships of human thenar motor units. J. Neurophysiol. 65:1509-1516.

Thomas, C. K.,Ross, B.H.,Stein, R.B.(1986) Motor-ut recruitment in human first dorsal interosseous muscle for static contractions in three different directions. J Neurophysiol, **55**.

Thompson CK, Negro F, Johnson MD, Holmes MR, McPherson LM, Powers RK, Farina D, Heckman CJ (2018) Robust and accurate decoding of motoneuron behaviour and prediction of the resulting force output. J.Physiol.(Lond.) 596:2643-2659.

Valente G, Crimi G, Vanella N, Schileo E, Taddei F (2017) nmsBuilder: Freeware to create subject-specific musculoskeletal models for OpenSim. Comput.Methods Programs Biomed. 152:85-92.

Van Cutsem M, Feiereisen P, Duchateau J, Hainaut K (1997) Mechanical properties and behaviour of motor units in the tibialis anterior during voluntary contractions. Can. J. Appl. Physiol. 22:585-597.

Van Cutsem M, Duchateau J, Hainaut K (1998) Changes in single motor unit behaviour contribute to the increase in contraction speed after dynamic training in humans. J.Physiol.(Lond.) 513:295-305.

Waasdorp R, Mugge W, Vos HJ, De Groot JH, Verweij MD, De Jong N, Schouten AC, Daeichin V (2021) Combining ultrafast ultrasound and high-density EMG to assess local electromechanical muscle dynamics: A feasibility study. Access 9:1.

Wallinga-De Jonge W, Gielen FL, Wirtz P, De Jong P, Broenink J (1985) The different intracellular action potentials of fast and slow muscle fibres. Electroencephalogr.Clin.Neurophysiol. 60:539-547.

Wexler AS, Jun Ding, Binder-Macleod SA (1997) A mathematical model that predicts skeletal muscle force. TBME 44:337-348.

Winters TM, Takahashi M, Lieber RL, Ward SR (2011) Whole muscle length-tension relationships are accurately modeled as scaled sarcomeres in rabbit hindlimb muscles. J.Biomech. 44:109-115.

Woittiez RD, Huijing PA, Boom H, Rozendal RH (1984) A three-dimensional muscle model: A quantified relation between form and function of skeletal muscles. J.Morphol. 182:95-113.

Wolters H, Wallinga W, Ypey DL, Boom HB (1994) Ionic currents during action potentials in mammalian skeletal muscle fibers analyzed with loose patch clamp. American Journal of Physiology-Cell Physiology 267:C1699-C1706.

Yushkevich PA, Piven J, Hazlett HC, Smith RG, Ho S, Gee JC, Gerig G (2006) User-guided 3D active contour segmentation of anatomical structures: Significantly improved efficiency and reliability. Neuroimage 31:1116-1128.

Zajac Felix E (1989) Muscle and tendon: Properties, models, scaling, and application to biomechanics and motor control. Critical reviews in biomedical engineering 17:359-411.

Zhao M, Hollingworth S, Baylor SM (1996) Properties of tri-and tetracarboxylate Ca2 indicators in frog skeletal muscle fibers. Biophys.J. 70:896-916.

Zot HG, Hasbun JE (2016) Modeling Ca2 -bound troponin in excitation contraction coupling. Frontiers in physiology 7:406.